Evaluation of single-footprint AIRS CH_4 Profile Retrieval Uncertainties Using Aircraft Profile Measurements

Susan S. Kulawik[1], John R. Worden[2], Vivienne H. Payne[2], Dejian Fu[2], Steve C. Wofsy[3], Kathryn McKain[4,5], Colm Sweeney[4], Bruce C. Daube, Jr[6], Alan Lipton[7], Igor Polonsky[7], Yuguang He[7], Karen E. Cady-Pereira[7], Edward J. Dlugokencky[8], Daniel J. Jacob[6], Yi Yin[9]

[1]BAER Institute, 625 2nd Street, Suite 209, Petaluma, CA, USA
[2]Jet Propulsion Laboratory, California Institute of Technology, Pasadena, CA, USA
[3]School of Engineering and Applied Sciences and Department of Earth and Planetary Sciences, Harvard University, Cambridge, MA 02138, USA
[4]National Oceanic and Atmospheric Administration, Earth System Research Laboratory, Boulder, CO, USA
[5]University of Colorado, Cooperative Institute for Research in Environmental Sciences, Boulder, CO, USA
[6]Harvard University, Cambridge, MA 02138, USA
[7]Atmospheric and Environmental Research, Inc., Lexington, Massachusetts, USA
[8]NOAA ESRL Global Monitoring Division, Boulder, Colorado
[9]California Institute of Technology

Correspondence to: Susan S. Kulawik (susan.s.kulawik@nasa.gov)

Abstract. We evaluate the uncertainties of methane optimal estimation retrievals from single footprint thermal infrared observations from the Atmospheric Infrared Sounder (AIRS). These retrievals are primarily sensitive to atmospheric methane in the mid-troposphere through the lower stratosphere (~2 to ~17 km). We compare to in situ observations made from aircraft during the Hiaper Pole to Pole Observations (HIPPO), the NASA Atmospheric Tomography Mission (ATom) campaigns, and from the NOAA ESRL aircraft network, between the surface and 5-13 km, across a range of years, latitudes between 60 S to 80 N, and over land and ocean. After a global, pressure dependent bias correction, we find that the land and ocean have similar biases and that the reported observation error (combined measurement and interference errors) of ~27 ppb is consistent with the standard deviation between aircraft and individual AIRS observations. A single measurement has measurement (noise related) uncertainty of ~17 ppb, a ~20 ppb uncertainty from radiative interferences (e.g. from water, temperature, etc.), and ~ 30 ppb due to "smoothing error", which is partially removed when making comparisons to in situ measurements or models in a way that account for this regularization. We estimate a 16 ppb validation error because the aircraft typically did not measure methane at altitudes where the AIRS measurements have some sensitivity, e.g. the stratosphere. Daily averaged AIRS measurements of at least 9 observations over spatio-temporal domains of < 1 degree and 1 hour have a standard deviation of ~17 ppb versus aircraft, likely because the observation errors from temperature and water vapor (for example) are only partly reduced through averaging. Seasonal averages can reduce this ~17 ppb uncertainty further to ~10 ppb, as determined through comparison with NOAA aircraft, likely because uncertainties related to radiative effects of temperature and water vapor can be reduced when averaged over a season.

1 Introduction

Advances in remote sensing, global transport modeling, and an increasingly dense network of surface measurements have led to substantive advances in evaluating the components and error structure of the global methane budget and the processes controlling this budget. For example, Frankenberg et al. (2005, 2011) showed that total column methane estimates could be derived from near infrared (NIR) radiances at ~1.6 microns measured by the Scanning Imaging Absorption Spectrometer for Atmospheric Cartography (SCIAMACHY). Since then, methane retrievals have also been applied to NIR radiances from the Greenhouse Gases Observing Satellite (GOSAT) instrument (e.g. Parker et al., 2011; Schepers et al., 2012), launched in 2009 with measurements, and the TROPOspeheric Monitoring Instrument (TROPOMI, e.g. Hu et al., 2018), launched in 2017. These data have sufficient accuracy to map regional surface methane enhancements (e.g. Kort et al., 2014; Wecht et al., 2014) and point source anomalies (Varon et al., 2019; Pandey et al., 2019). Estimates of the free-tropospheric methane concentrations from spaceborne measurements in the thermal infrared (TIR) at ~8 microns were demonstrated using radiances from the Aura Tropospheric Emission Spectrometer (TES, Worden et al., 2012; 2013b), the Atmospheric Infrared Sounder (AIRS, e.g. Xiong et al., 2013), the Infrared Atmospheric Sounding Interferometers (IASI, e.g. Ravazi et al., 2009; De Wachter et al., 2017; Siddans et al., 2017), the Cross-Track Infrared Sounders (CrIS, e.g. Smith and Barnet, 2019) and TIR GOSAT measurements (de Lange and Landgraf, 2018). TIR methane measurements have been used to evaluate the role of fires (e.g. Worden et al., 2013b; 2017a), Asian emissions and stratospheric intrusions (e.g. Xiong et al., 2009; 2013) on the global methane budget.

The goal of this paper is to evaluate the uncertainties of new methane retrievals from AIRS single footprint, original (non-cloud-cleared) radiances using aircraft measurements from the HIAPER Pole-to-Pole Observations (HIPPO) and Atmospheric Tomography Mission (ATom) campaigns and National Oceanic and Atmospheric Administration (NOAA) Earth System Research Laboratory (ESRL) aircraft network, taken between 2006 and 2017. Evaluation of these uncertainties are needed to determine if AIRS methane data can characterize and improve errors in global chemistry transport models. For example, a recent paper by Zhang et al. (2018) combined synthetic CrIS and TROPOMI methane retrievals and a global inversion system to show that it would be possible to infer the north-south gradient of OH, the primary methane sink, to within 10%, and temporal variations of OH concentrations. However, knowing the accuracy of the methane data is important for inferring the uncertainty in the spatio-temporal variability of OH. Over decadal time scales, OH can vary by 3-5% (e.g. Turner et al., 2018a, 2018b, 2019; Rigby et al., 2017). Therefore, to be useful for understanding OH, monthly or seasonally averaged AIRS data should have an uncertainty that is less than 3-5% (55-99 ppb).

In this paper we present an evaluation of methane retrievals derived from AIRS single footprint radiances. We follow an optimal estimation approach (Rodgers, 2000), based on the heritage of the Aura Tropospheric Emission Spectrometer (TES) algorithm (Bowman et al., 2006), now called the MUlti-SpEctra, MUlti-SpEcies, MUlti-Sensors (MUSES) algorithm (Worden et al., 2006, 2013b; Fu et al., 2013, 2016, 2018, 2019). MUSES uses radiances from one or multiple instruments to quantify and characterize geophysical parameters derivable from those radiances. The optimal estimation method provides the vertical sensitivity (i.e., the averaging kernel matrix) and estimates of the uncertainties due to noise and to radiative interferences such

as temperature, N2O, and water vapor. We compare AIRS retrievals with corresponding aircraft data over a range of latitudes and longitudes in order to evaluate the calculated uncertainties over ocean and land. Much of the description of the forward model and retrieval approach is provided in Worden et al. (2012, 2019). We therefore refer the reader to these papers for a more in depth description of the retrieval approach and only summarize aspects here that are relevant for comparing the AIRS methane retrievals to aircraft data.

2 Datasets used in this paper

The quantities of interest that we validate in this paper are a) the AIRS CH_4 dry volume mixing ratio (VMR) at particular pressure values between 750 hPa and 300 hPa, or b) the AIRS CH_4 dry VMR partial column covering the same pressure range that is measured by the aircraft. We use aircraft profiles which span the pressure range that contains at least 0.20 degrees of freedom for the AIRS CH_4 partial column.

2.1 Description of AIRS

The AIRS instrument is a nadir-viewing, scanning infrared spectrometer (Aumann et al., 2003; Pagano et al., 2003; Irion et al., 2018; DeSouza-Machado et al., 2018) that is onboard the NASA Aqua satellite and was launched in 2002. AIRS measures the thermal radiance between approximately 3-12 microns with a resolving power of approximately 1200. For the 8 micron spectral range used for the HDO/H_2O/CH_4 retrievals, the spectral resolution is ~1 wavenumber (cm-1), with a gridding of ~0.5 cm-1, and the signal-to-noise (SNR) ranges from ~400 to ~1000 over the 8 micron region for a typical tropical scene. A single footprint has a diameter of ~15 km in the nadir; given the ~1250 km swath, the AIRS instrument can measure nearly the whole globe in a single day. The Aqua satellite is part of the "A-Train" that consists of multiple satellites and instruments, including TES, in a sun-synchronous orbit at 705 km with an approximately 1:30 am and 1:30 pm equator crossing-time. In this paper, we use only daytime data to match the validation observations.

1.2 Overview of Aircraft Data

Measurements from the HIPPO and ATom aircraft campaigns (Wofsy et al., 2012) provide an excellent data set for satellite validation, due to the wide latitudinal coverage, the large vertical extent of the profiles (up to 9-12 km), and the availability of campaigns over a wide range of months. Each of the five HIPPO campaigns flew south, then north over a period of weeks, often using a different path for the northern and southern legs, with campaign dates in 2009 - 2011. Atmospheric methane concentrations were measured with a quantum cascade laser spectrometer (QCLS) at 1 Hz frequency with accuracy of 1.0 ppb and precision of 0.5 ppb (Santoni et al., 2014). HIPPO methane data are reported on the WMO X2004 scale and have been used in several other studies to evaluate satellite retrievals of methane (e.g. Alvarado et al., 2015; Wecht et al., 2012; Crevoisier et al., 2013). Comparisons with NOAA flask data showed a mean positive bias of 0.85 ppb for the QCLS during the HIPPO campaigns, which is consistent with the estimated QCLS accuracy of 1.0 ppb (Santoni et al., 2014; Kort et al., 2011). We used

396 QCLS CH_4 profiles from the HIPPO campaigns. Using coincidence criteria of ±9 hours, ±50 km, 22,271 AIRS observations were processed, of which 5537 passed quality flags. The latitude of the matches ranges from 57S to 81N.

We compare AIRS to observations from the ATom aircraft campaigns 1-4 (Wofsy et al., 2018). This comparison provides validatation ~7 years after HIPPO, between 2016 and 2018. Similar to HIPPO, these observations include observations in the Pacific Ocean, but ATom also includes observations in the Atlantic (as seen in Table A.1 and Fig. 1). ATom methane data are reported on the WMO X2004A scale. We used 289 profiles from the ATom campaigns from the NOAA Picarro instrument (Karion et al., 2013). For more information on the instrument, see https://espo.nasa.gov/sites/default/files/archive_docs/NOAA-Picarro_ATom1234_readme.pdf. Using coincidence criteria of ±9 hours, ±50 km, 21,225 AIRS observations were processed, of which 4913 passed quality flags. The latitude of the matches ranges from 65S to 65N.

The NOAA ESRL aircraft network observations (Cooperative Global Atmospheric Data Integration Project, 2019) are taken twice per month at fixed sites primarily in North America, and also Rarotonga (RTA) at 21S (Sweeney et al., 2015, http://dx.doi.org/10.1002/2014JD022591). NOAA aircraft network methane data are reported on the WMO X2004A scale. Although HIPPO data are not reported on the same scale as ATom and NOAA aircraft network data, differences in values of calibration tanks used for HIPPO (Santoni et al., 2014) on the two different scales are < 1 ppb. We match AIRS and aircraft observations between 2006 and 2017, with coincidence criteria of 50 km, 9 hours, finding ~43,000 matches, and 18,000 good quality matches following the retrieval, to 719 aircraft measurements, at sites ACG (67.7N, 164.6E, 401 matches), ESP (49.4N, 126.5E, 2743 matches), NHA (43.0N, 70.6E, 2682 matches), THD (41.1N, 124.2E, 1551 matches), CMA (38.8N, 74.3E, 3269 matches), TGC (27.7N, 96.9E, 1944 matches), and RTA (21.2S, 159.8E, 810 matches).

Figure 1 shows the locations of all the aircraft data used for the comparisons described in this paper. Most of the ocean measurements are from the HIPPO and ATom campaigns that spans a range of latitudes, whereas most of the land measurements are taken over North America..

3 MUSES-AIRS Optimal Estimation of CH_4 from single-footprint, original (non-cloud-cleared) AIRS radiances

Worden et al. (2012, 2019) describe in detail the forward model and retrieval approach used for estimating methane from TES and AIRS radiances. The radiative transfer forward model used for this work is the Optimal Spectral Sampling (OSS) fast radiative transfer model (RTM) (Moncet et al., 2005, 2008, 2015). In particular, radiances from the thermal infrared bands at 8 and 12 microns are used to quantify profiles of atmospheric concentrations of CH_4, HDO, H_2O, N_2O, as well as temperature, emissivity, and cloud properties. Since we use optimal estimation, or O[illegible] (e.g. Rodgers, 2000; Bowman et al., 2006) to estimate these quantities we can characterize the vertical resolution and uncertainties of these retrievals, which allows us to

compare them to models and independent data sets, while accounting for the regularization used for the retrieval. We follow the OE approach for the Aura TES instrument (e.g. Bowman et al., 2006; Worden et al., 2006, 2012) but with some differences. First, methane retrievals using the TES radiances are obtained using only the 8 micron band, because of slight calibration differences between the detectors that measure the 12 and 8 micron bands (e.g. Shephard et al., 2008; Connor et al., 2011). For the AIRS retrievals, we use both the 8 and 12 micron bands in order to better constrain temperature in the troposphere and stratosphere. Secondly, the TES based retrieval uses the ratio of a jointly-retrieved N2O profile to the CH_4 profile in order to help correct biases related to temperature variations in the (UTLS) upper-troposphere lower-stratosphere (Worden et al., 2012). However, the N2O correction is not used for the AIRS retrievals because we can jointly estimate temperature in the UTLS region using the 12 micron band. We use similar quality flags as the TES retrievals such as checks on the χ^2, residual signal, and cloud optical depth as discussed in Kulawik et al. (2006a, 2006b), except that we screen out cloudy and low-sensitivity cases, resulting in about 1/4 of the data passing screening. The specific flags used for AIRS CH_4 are as follows:

Good quality and sensitivity flagging for AIRS CH_4

Radiance residual rms < 1.5. This screens off the standard deviation of the radiance residual (the difference between the observed and fit radiance normalized by the NESR).

|Radiance residual mean| < 0.15. This screens off the mean difference of the radiance residual.

|KdotdL| < 0.23. This screens off the dot product of the Jacobians and the radiance residual and indicates that there is little remaining information relative to the noise level about the surface and atmosphere in the retrieval

TSUR < near-surface atmospheric temperature value + 30K. This ensures that the thermal gradient is less than 30K.

Cloudtop pressure > 90 hPa. This ensures that the retrieved cloudtop is not above 90 hPa.

Cloud OD < 0.3. This ensures that the cloud is not opaque and there is sensitivity below the cloud.

Cloud variability versus wavenumber < 1.5 * cloud OD. This ensures that the cloud optical depth does not vary too much with wavenumber.

Degrees of freedom > 1.1. This ensures a minimum sensitivity.

Tropospheric degrees of freedom > 0.7. This ensures a minimum Tropospheric sensitivity.

Stratospheric degrees of freedom < 0.5. This ensures that there is not too much sensitivity in the stratosphere.

Predicted error on the column above 750 hPa < 53 ppb. This ensures that the predicted error is not too large.

3.1 Retrieval Error Characteristics

Detailed descriptions of the use of optimal estimation (OE) to infer trace gas profiles from remote sensing radiance measurements retrieval is included in numerous publications (e.g. Rodgers, 2000; Worden et al., 2006; Bowman et al., 2006). However, we present a partial description here as it is relevant for comparing the AIRS methane retrievals and aircraft profile measurements. As discussed in Rodgers (2000), the estimate for a trace gas profile inferred (or inverted) from a radiance spectrum is described by the following linear equation:

$$\hat{\mathbf{x}} = \boldsymbol{x}_a + \mathbf{A}(\mathbf{x} - \boldsymbol{x}_a) + \mathbf{G_R}\sum_i \mathbf{K_i^b}(\mathbf{b}_i - \mathbf{b}_i^a) + \mathbf{Gn} \quad \textbf{(1)}$$

where x^_is the estimate of Log(VMR), ⟦x_⟧_a^ is the log of the a priori concentration profile used to regularize the inversion. We split x into [x,y], where x is the quantity of interest, the methane profile, and y are the jointly estimated quantities (such as temperature, water vapor, clouds, and surface properties), which results in the cross-state error (Worden et al., 2004; Connor et al., 2008).

$$\hat{\mathbf{x}} = \boldsymbol{x}_a + \mathbf{A}_{xx}(\mathbf{x} - \boldsymbol{x}_a) + \mathbf{G_R}\sum_i \mathbf{K_i^b}(\mathbf{b}_i - \mathbf{b}_i^a) + \mathbf{A}_{xy}(\mathbf{y} - \boldsymbol{y}_a) + \mathbf{Gn} \quad \textbf{(2)}$$

For the AIRS (and TES) OE methane retrievals, $\mathbf{x}_a$ comes from the MOZART atmosphere chemistry model (e.g. Brasseur *et al.*, 1998). The vector **x** is the "true state", or in this case the (log) concentration profile. The matrix **A** is the averaging kernel matrix or $\mathbf{A} = \frac{\partial \hat{x}}{\partial x}$ and describes the vertical sensitivity of the measurement. The matrix **G** relates changes in the radiance (**L**) to perturbations in **x,** $\mathbf{G} = \frac{\partial x \partial L}{\partial L \partial x}$. The vector **n** is the noise vector, the matrix **K** is the sensitivity of the radiance to changes in (log) concentration $\mathbf{K} = \frac{\partial L}{\partial log(x)} = \frac{\partial L}{\partial log(VMR)}$, and the set of vectors $\mathbf{b}_i$ represent interference errors not estimated from the observed radiances. The true state, noise vector, and interference errors as described here are the "true" values and are therefore not actually known but are represented in this form so that we can calculate how their uncertainties affect the estimate $\hat{\boldsymbol{x}}$. An example averaging kernel matrix is shown in Figure 2 and shows that AIRS based estimates of methane are most sensitive to methane in the free-troposphere and lower-stratosphere as demonstrated previously for AIRS and other TIR based estimates of tropospheric methane (e.g. Xiong *et al.*, 2016; de Lange and Landgraf, 2018).

Finally, we look at the quantity of interest, $\hat{x} = \mathbf{hx}$. The vector **h** combines all the necessary operations that maps the (log) concentration profiles to whatever quantity is needed such as selecting one particular pressure level (e.g. **h**= [0,0,0,1,0,0,0, …], selecting a column average, (**h** = pressure weighting function) – see Connor et al., 2008) or selecting the VMR mean (e.g. **h**=1/m, where m is the number of pressure levels to average).

$$\hat{x} = \mathbf{h}\hat{\mathbf{x}} \quad \text{(3a)}$$

$$\hat{x} = \mathbf{hx}_a + \mathbf{hA}_{xx}(\mathbf{x} - \mathbf{x}_a) + \mathbf{hG_R}\sum_i \mathbf{K_i^b}(\mathbf{b}_i - \mathbf{b}_i^a) + \mathbf{hA}_{xy}(\mathbf{y} - \boldsymbol{y}_a) + \mathbf{hGn} \quad \text{(3b)}$$

In Eq. 3a, the vector $\hat{\mathbf{x}}$ (denoted in bold) is converted to the scalar of interest, $\hat{x}$ (non-bold, italic). In our validation comparisons, **h** is used to select 1) a specific pressure level that is measured by the aircraft, 2) the partial column average over the pressure levels measured by the aircraft, and 3) the partial column above 750 hPa.

3.2 Approach for Comparing AIRS measurements to aircraft profiles

A challenge in comparing the satellite-based AIRS measurements to aircraft data is that the aircraft will typically measure only a section of the atmosphere (e.g. the troposphere), whereas the AIRS measurements are sensitive, to varying degrees (see Fig. 2), to the entire atmosphere. To account for these differences, we divide the atmosphere into two parts $\mathbf{x} = [\mathbf{x}_c, \mathbf{x}_s]$: where $\mathbf{x}_c$ is the part measured by the aircraft (denoted **c** for airCraft), and $\mathbf{x}_s$ is the part not measured by the aircraft (denoted **s** for Stratospheric):

$$\hat{x}_c = \mathbf{h}_c\mathbf{x}_a + \mathbf{h}_c\mathbf{A}_{cc}(\mathbf{x}_c - \boldsymbol{x}_a^c) + \mathbf{h}\mathbf{G}_\mathbf{R}\sum_i \mathbf{K}_\mathbf{i}^\mathbf{b}(\mathbf{b}_i - \mathbf{b}_i^a) + \mathbf{h}_c\mathbf{A}_{cy}(\mathbf{y} - \boldsymbol{y}_a) + \mathbf{h}_c\mathbf{A}_{cs}(\mathbf{x}_s - \boldsymbol{x}_a^s)\mathbf{A}_{cs}(\mathbf{x}_s - \boldsymbol{x}_a^s) + \mathbf{h}_c\mathbf{G}\mathbf{n} \quad \textbf{(4)}$$

where the term $\mathbf{A}_{cs}$ is the cross-term in the averaging kernel that describes the partial derivatives of the aircraft-measured levels (e.g. the troposphere) to the un-measured levels (e.g. the stratosphere). Equation 4 describes how the AIRS measurement $\hat{x}_c$ responds to the true state $[\mathbf{x}_c, \mathbf{x}_s]$.

We compare our AIRS observation, $\hat{x}_c$ in Eq. 4, to our aircraft observation, $\boldsymbol{x}_{aircraft}$. To compare directly to the aircraft observation (without accounting for AIRS sensitivity) we would compare to $\hat{\boldsymbol{x}}^c_{aircraft} = \mathbf{h}_c\boldsymbol{x}_{aircraft}$. However, the expected error would include smoothing error which is estimated to be 30 ppb. In Equation 5a, we first apply the AIRS Averaging kernel to the aircraft measurement to account for the AIRS sensitivity:

$$\hat{\boldsymbol{x}}^c_{aircraft} = \mathbf{h}_c\mathbf{x}_a + \mathbf{h}_c\mathbf{A}_{cc}\left(\mathbf{x}^c_{aircraft} - \boldsymbol{x}_a^c\right) + \mathbf{h}_c\mathbf{A}_{cs}\left(\mathbf{x}^s_{aircraft} - \boldsymbol{x}_a^s\right) \quad \textbf{(5a)}$$

One issue is that we do not actually have aircraft observations in the "s" part of the atmosphere, $\mathbf{x}^s_{aircraft}$, which is used in the second term of Eq. 5a. We have aircraft observations in the "c" part of the atmosphere only, so we apply the Averaging Kernel to this part of the atmosphere only:

$$\hat{\boldsymbol{x}}^c_{aircraft} = \mathbf{h}_c\boldsymbol{x}_a + \mathbf{h}_c\mathbf{A}_{cc}\left(\boldsymbol{x}^c_{aircraft} - \boldsymbol{x}_a^c\right) \quad \textbf{(5b)}$$

Equation 5a accounts for the AIRS smoothing error, whereas Equation 5b (the equation used in this work) only accounts for the smoothing error from the part of the atmosphere measured by the aircraft profile. The difference from Eqs. 5a and 5b is discussed in Section 3.3.

The expected difference between $\hat{x}_c$ (the measured AIRS value) and $\hat{\boldsymbol{x}}^{\boldsymbol{c}}_{\boldsymbol{aircraft}}$ (the aircraft value with the AIRS Averaging kernel applied) is calculated from Eqs. 4 and 5b:

$$\mathbf{E}||\ (\hat{\mathbf{x}}_c - \hat{\boldsymbol{x}}^{\boldsymbol{c}}_{\boldsymbol{aircraft}})|| = \mathbf{h}_c(\mathbf{A_{cb}}\mathbf{S_a^{bb}}\mathbf{A_{cb}^T} + \mathbf{A_{cy}}\mathbf{S_a^{yy}}\mathbf{A_{cy}^T} + \mathbf{A_{cs}}\mathbf{S_a^{ss}}\mathbf{A_{cs}^T} + \mathbf{S_m^{cc}})\mathbf{h}_c^T \quad \textbf{(6)}$$

The matrix $\mathbf{S_a}$ term describes the *a priori* uncertainty of methane, interferents, or systematic parameters, which propagate into the error in the first 3 terms: (1) $\mathbf{A_{cb}}\mathbf{S_a^{bb}}\mathbf{A_{cb}^T}$ describes systematic error, e.g. due to spectroscopy and calibration; these likely impart biases into the AIRS measurement which are characterized during validation, (2) $\mathbf{A_{cy}}\mathbf{S_a^{yy}}\mathbf{A_{cy}^T}$ describes the "cross-state error", the effect of jointly retrieved parameters like temperature onto methane, (3) $\mathbf{A_{cs}}\mathbf{S_a^{ss}}\mathbf{A_{cs}^T}$ describes the impact of the part of the atmosphere not covered by the aircraft on the measured section: this must be included because the AIRS measurement sees a combination of both parts of the atmosphere and cannot completely disentangle them. The final term, $\mathbf{S_m^{cc}}$, is the measurement error, which is the propagation of radiance error into the retrieved parameters, and is $\mathbf{G_c}\ \mathbf{S_n}\ \mathbf{G_c^T}$, where $\mathbf{G_c}$ is the gain matrix and $\mathbf{S_n}$ is the covariance of the radiance error, in our case, a diagonal matrix. The error covariances all represent fractional errors, in log(VMR). The error in ppb is approximately the fractional error times the methane value in ppb.

For the purpose of evaluating the AIRS methane measurement uncertainties and comparing the AIRS methane to aircraft in situ measurements we refer to the four terms on the right side of Eq. 6 as:

1) $\mathbf{S_b^{cc}}$ is the systematic error due to terms that are not accounted for in the retrieval state vector, such as spectroscopy and calibration; these terms are estimated by comparisons with the aircraft data. A pressure-dependent bias correction, described in Section 3.4, of approximately -60 ppb is used to correct this systematic bias.
2) $\mathbf{A_{cy}}\mathbf{S_a^{yy}}\mathbf{A_{cy}^T}$, the "cross-state", which is included in the MUSES-AIRS methane estimate product files, and is the propagation of temperature, water vapor, and cloud errors into AIRS. The errors in the retrieved temperature and water vapor at nearby location are correlated over short spatio-temporal scales, as described in Section 4, and so this error does not reduce with averaging nearby observations. However, monthly or seasonal averages reduces cross-state error, because systematic errors from temperature / water / cloud can be assumed to vary pseudo-randomly over larger time scales. We estimate this error as ~21 ppb (see next paragraph).
3) $\mathbf{A_{cn}}\mathbf{S_a^{nn}}\mathbf{A_{cn}^T}$ is the "validation uncertainty" due to knowledge uncertainty of the stratosphere although this may also contain other levels that are also not measured by the aircraft. This is the smoothing error which cannot be removed from the comparisons because the aircraft does not make measurements at the "**n**" (**n**ot measured) levels. We estimate this validation error as ~16 ppb (see next section).

4) $\mathbf{S_m^{cc}}$, the "measurement" error, which is included in the AIRS methane estimate product files. The measurement error is random and is expected to reduce as the inverse square root of the number of observations averaged. We estimate this error as ~18 ppb (see next paragraph)

Figure 3 shows the predicted errors for the AIRS partial column matching the aircraft measurements. The measurement error (light green) is 18 ppb, the cross-state error is 21 ppb (red minus green in quadrature), and the total error for a single observation (including smoothing error) is 41 ppb. The errors not shown in this plot are the validation error, estimated in the next section, and systematic error, which we remove with a bias correction in Section 3.4.

3.3 Estimating validation error due to aircraft not measuring the stratosphere

A typical aircraft profile will only measure part of the troposphere and rarely measure into the stratosphere. However, the AIRS methane profile measurements are sensitive to methane variations over the whole atmosphere as shown by the averaging kernel matrix in Figure 2. Options for dealing with this are a) extending the true with the AIRS prior or b) extending the true with a model profile value. Note that models in general have a positive bias in the extratropical stratosphere (Patra et al., 2011). In GEOS-Chem 4x5, the column bias is shown in Figure 2c of Turner et al. (2015) and further discussed in Maasakkers (2019), which finds a bias in the stratosphere.

This section estimates this uncertainty by calculating the difference of $\boldsymbol{x}^{\boldsymbol{c}}_{\boldsymbol{aircraft}}$ for Eq. 5a minus Eq. 5b when extending the aircraft using two different "true" profiles taken from two different global atmospheric chemistry models, the Laboratoire de Météorologie Dynamique (LMDz) model (e.g. Folberth et al., 2006) model and the Goddard Earth Observing System (GEOS-Chem) model (e.g. Maasakkers et al., 2019). So, if the model value equaled the AIRS prior in the stratosphere, this difference would be zero. The differences for $\boldsymbol{x}^{\boldsymbol{c}}_{\boldsymbol{aircraft}}$ from LMDz model and GEOS-Chem are shown in Figure 4 for all HIPPO ocean and land data; these differences show that model/model differences in the stratosphere can contribute significantly to the differences between AIRS and aircraft validation.

These differences provide an estimate for how knowledge error in the stratosphere projects to uncertainties in our methane retrievals. For example, this uncertainty varies with latitude, similar to the residual bias between the AIRS estimate and aircraft (next section). Furthermore, the variability over small latitudinal ranges of 10 degrees or less suggests that the random part of the stratospheric error is smaller than this latitudinal variability. Our 16 ppb estimate for this error is similar to the 10 ppb estimate for the impact of stratospheric uncertainty on column estimates from aircraft profiles (Wunch et al., 2010). Appendix A shows further analysis of mean differences of AIRS minus aircraft for different profile extension choices.

3.4 Bias Correction

AIRS CH_4 shows a persistent high bias of 25 to 90 ppb versus aircraft observations in Fig. 6. Previous studies using remotely sensed measurements suggest that a bias correction to the AIRS methane profile measurement must account for the vertical sensitivity (e.g. Worden et al., 2011). For example, in the limit where the AIRS measurement is perfectly sensitive to the vertical distribution of methane, the bias correction could be a simple scaling factor. However, in the limit where the AIRS measurement is completely insensitive (e.g. DOFS = 0.0) then the bias correction is zero. We therefore use the bias correction approach described in Worden et al. (2011), which passes a bias correction through the averaging kernel to account for the AIRS sensitivity.

We use HIPPO-4 observations to set a bias correction which we then evaluate with the other HIPPO campaigns and NOAA aircraft network data. To set the bias, we use Eq. 5 to estimate the aircraft observation as seen by AIRS, then compare this to AIRS observations. The result (by pressure level) is shown in Table 1. Then a bias was applied to AIRS using Eq. 7, with the bias term δ_{bias} in the form of Eq. 8.

$$\boldsymbol{ln}(\hat{\boldsymbol{x}}_{\boldsymbol{corrected}}) = \boldsymbol{ln}(\hat{\boldsymbol{x}}_{\boldsymbol{orig}}) + \mathbf{A}(\boldsymbol{\delta}_{\boldsymbol{bias}}) \quad \textbf{(7)}$$

Where ln() is the natural log, because the retrieved quantity is ln(VMR). We fit a single bias function for all AIRS measurements by minimizing the difference between the AIRS and HIPPO-4 with δ_bias constrained to have a slope with pressure, and two pressure domains. We specify that δ_bias cannot jump more than 0.05 (5%) between the two domains.

$$\delta_{bias} = c + dP \ (\mathrm{P} > \mathrm{P_o})$$
$$\delta_{bias} = e + fP \ (\mathrm{P} < \mathrm{P_o}) \quad \textbf{(8)}$$

where P is pressure in hPa. The optimized bias correction parameters were: c = 0.0; d = - 6.1e-5; Po=400 hPa; e=-0.09; f=0.00018. This bias correction results are shown for HIPPO-4; HIPPO-1,2,3,5; and NOAA observations in Table 1. The remainder of the paper, unless specified, uses data bias-corrected by Eqs. 7 and 8.

Figure 5 shows the effect of bias correction on the average of all HIPPO 1,2,3,5 AIRS profiles. The bias correction improves the mean AIRS / aircraft difference and improves the pressure-dependent skew in the bias (Table 1). The HIPPO data is shown before and after the AIRS averaging kernel is applied (using Eq. 5), which has the effect of bringing the HIPPO observations towards the AIRS prior. This is to match the imperfect sensitivity of satellite-based observations, which are similarly influenced by the prior.

4 Evaluation against aircraft data by latitude

4.1 Comparison of aircraft observations with and without bias correction

Figure 6 shows a comparison between all AIRS measurements within 50 km and 9h of an aircraft measurement for the partial column measured by the aircraft. There is a mean bias of 57 ppb overall, ~56 ppb for ocean and ~64 ppb for the land. The RMS difference is ~27 ppb. Furthermore, there appears to be latitudinal variations in the bias. For example, the mean difference between the AIRS and aircraft over the ocean for latitudes less than 20 S is ~74 ppb and for latitudes between 20 S and 20 N this bias is ~ 56 ppb.

Figure 7 shows the same comparisons as Fig. 6 after bias correction (described in Section 3.4). The mean bias is 1 ppb, and the RMS difference is 24 ppb. The overall land bias is 13 ppb, and the overall ocean bias is 1 ppb (shown in Table A.1). Note that the HIPPO land observations are primarily in Australia, New Zealand, and North America, whereas the ocean comparisons are in the mid-Pacific, as seen in Fig. 1. We expect the RMS difference to be similar to the observation error, as the terms that make up the observation error are the primary source of variability in the observations (e.g. Worden et al., 2017b). The predicted observation error from Fig. 3, is 27 ppb, and is consistent with the RMS difference seen here, 24 ppb. However, knowledge of the stratosphere / validation error is potentially a large component of the latitudinal variability in the difference seen in the bottom panel of Fig. 7.

We also compare to NOAA aircraft network and ATom observations and find similar results as HIPPO. Figure 8, discussed in Section 4.2, shows ATom results, and Figure 9, discussed in Section 4.2, shows comparisons to a NOAA aircraft time series. The biases for different pressure ranges, campaigns, and surfaces is shown in Table A.1. Table A.3 shows the standard deviation of AIRS minus validation by pressure and surface type, for single observations, daily, and seasonal averages.

4.2 Errors in averaged AIRS data

Satellite data are typically averaged in order to improve the precision of a comparison between data and model. However, as shown in the previous figure, these data contain errors that vary with latitude. For example, knowledge error of the true profile in the stratosphere as well as errors in the jointly retrieved AIRS temperature and water vapor retrievals have both a random and a bias component, both of which vary with latitude. The bias component is approximately the same for all AIRS methane measurements taken at roughly the same location and time as we do not expect large variations in temperature and water vapor errors over these scales. To quantify the component of the accuracy that cannot be reduced by averaging, we compare averages of AIRS measurements to HIPPO and ATom measurements. We average the daily matches, which contain at least 9 AIRS observations matching a single HIPPO or ATom measurement, within +-50 km of the measurement. The number of AIRS observations averaged ranges from 9 to 53 and averages 20. We specify that there needs to be at least 9 AIRS observations for each comparison so that the systematic error, and not the precision (or measurement error) , is the dominant term. Figure 8

shows the average predicted error, assuming that the error is random, e.g. if 20 observations were averaged, this would equal 24 / √20 ppb or ~ 5 ppb. The standard deviation between the averaged AIRS and HIPPO or ATom data is ~17 ppb. Note that same-colored adjacent points (i.e. adjacent observations from the same campaign) often show similar biases. Because this RMS difference is much larger than what is expected if the errors were purely random, this shows the presence of systematic errors, either in the AIRS data or in the validation error. We therefore report 17 ppb as the limiting error when averaging AIRS data within one-degree grids and 1 day for the purpose of comparing to models or other methane profiles.

On the other hand, averaging AIRS data seasonally can reduce the error further because geophysical errors from as temperature and water vapor vary over longer time scales. We demonstrate this aspect of the AIRS uncertainties by comparing averaged AIRS data to the NOAA aircraft methane profiles taken off the coast near Corpus Christi, Texas (27.7N, 96.9W, site TGC). We screen for at least 3 observations per day, less than the 9 observations/day used for HIPPO / ATom daily averages in order to get enough daily averages to explore how the errors reduce with monthly and seasonal averages, since the aircraft make 1-2 measurements per month. Figure 9 shows daily, monthly, 90-day, and seasonal averages of the partial column matching the aircraft measured column at TGC. The seasonal averages are created by converting all AIRS/aircraft matched pairs to 2012 by adding 5.4 ppb per year multiplied by (year minus 2012), then averaging all values within each month. Similarly to the findings for HIPPO and ATom, the daily error is much larger than predicted from the observation error with the assumption of randomness. The standard deviation of AIRS minus aircraft at TGC is 24 ppb (for single AIRS observation, not shown), 11.5 ppb (for daily AIRS average, (Figure 9a)). The predicted error with the assumption that the error is random, is 6.0 ppb. Therefore, similarly to the ATom and HIPPO findings, the errors within small geophysical region are correlated and do not average as the square root of the number of observations. However, next, we try averaging multiple days within 1 month, and find a standard deviation of for monthly averages of at least 2 days of 8.2 ppb (Figure 9b), and the standard deviation of 3-month averages containing at least 3 days, 6.2 ppb (Figure 9c). These agree with the predicted errors of 8.0 and 6.0 ppb, respectively, by taking the daily standard deviation (11.5 ppb) and dividing by the square root of the number of days averaged. The seasonal cycle average, which is a monthly average of all matched pairs from any year, has a standard deviation of 5.9 ppb, whereas the predicted error, from the daily average divided by the square root of number of observations, is 4.2 ppb.

Appendix A, Table A.3 shows the standard deviation for all NOAA ESRL stations, for ocean and land AIRS observations. The ocean vs. land observations show similar values, with land and ocean standard deviations within 2 ppb. A single land observation has a standard deviation versus aircraft observations of 23 ppb for the partial column, in agreement with predicted observation error of 23 ppb. The standard deviation for daily observations is 15.2 ppb, whereas the predicted error, using 23 ppb divided by the square root of the number of observations averaged, is 5.9 ppb, indicated correlated errors when averaging nearby observations. The monthly standard deviation is 10.9, in reasonable agreement with the predicted of 9.4 ppb, from the daily average standard deviation divided by the number of observations averaged. The seasonal cycle average, which is a monthly average of all matched pairs from all years, has a standard deviation of 7.7 ppb, which is similar to the predicted error

of 6.9 ppb, from the daily average divided by the square root of number of observations. We find that estimating the error as the daily standard deviation divided by the square root of the number of days averaged is a reasonable estimate of the actual error.

5 Discussion and Conclusions

We validate single-footprint AIRS methane by comparing 27,000 AIRS methane retrievals to 396 aircraft profiles from the HIPPO campaign, 719 profiles from the NOAA ESRL aircraft network, and 289 aircraft profiles from the ATom campaign, taken across a range of latitudes, longitudes, and times. The AIRS methane retrievals are derived using the MUSES optimal estimation algorithm that has previously been applied to Aura TES radiances (e.g. Fu et al., 2013). After adjusting the aircraft profile to account for the AIRS sensitivity (using the averaging kernel and a priori profile), we compare the mean methane value over the aircraft profile to the mean methane from the AIRS profile over the same altitude (or pressure) range. We use a subset of validation data to derive a pressure-dependent bias correction on the order of -60 ppb, and test this on an independent set of validation data. After the bias correction, we report a bias of 0 +/- 10 ppb. The bias between AIRS and aircraft varies with pressure and location, as seen in Appendix A.

After applying the bias correction, from Eq. 7 and 8, the RMS difference between the AIRS and aircraft data of the partial column matching the aircraft of ~22 ppb is consistent with the mean observation error, composed of random error from noise and the cross-state errors from jointly retrieved temperature, water vapor, clouds, and surface parameters that are projected onto the AIRS methane retrieval. The extent to which the aircraft profiles used here can be utilized as "truth" for the purposes of validation is limited by knowledge of the methane profile above the aircraft profile (referred to here as "validation error") which limits our knowledge of "truth" to within about 16 ppb. This uncertainty is consistent with the location-dependent bias in the satellite/aircraft comparisons which can vary by ~10 ppb.

We quantify the AIRS minus validation standard deviation for single observations, daily averages (within 50 km of the validation location), monthly averages, and seasonal averages for data bias corrected using Eqs. 7 and 8. The AIRS minus validation standard deviations are: 24 ppb (single AIRS footprint), 17 ppb (daily AIRS averages within 1 degree latitude and longitude), 10 ppb ("monthly" AIRS averages), 9 ppb (3-month AIRS average), and 7 ppb (seasonal cycle average). The errors on averaged AIRS data are likely an upper bound on the AIRS error, due to the uncertainty in the validation. The single-footprint and daily average standard deviations for different pressure ranges and surface types are shown in Appendix A. We recommend using the standard deviations in this paragraph as the error budget for the specified averaged quantities.

These results can be compared to AIRS v6 validation by Xiong et al. (2015), which validated AIRS CH_4 retrieved from cloud-cleared radiances on the 9-footprint 45 km field of regard. Xiong et al. (2015) finds AIRS standard deviations versus HIPPO

of 0.9% (16 ppb) for pressures between 575 and 777 hPa, 1.2 % (18 ppb) standard deviation for pressures between 441 and 575 hPa, and 1.6% (29 ppb) between 343 and 441 hPa. Xiong et al. (2015) also found a pressure-dependent bias, with a -25 ppb bias near the top of the troposphere, and a high 5 ppb bias near the mid-Troposphere.

5 Appendix A: Biases and standard deviations for different stations, campaigns, pressures, and surface types

We characterize the bias versus validation data by station, campaign, and pressure level. Table A.1 shows biases versus validation data, after bias correction with Eq. 7. In the HIPPO comparisons, the biases are generally smaller than about 10 ppb. There is no overall pattern in the bias by season. The land data is biased higher than ocean for HIPPO comparisons (about +20 ppb). However, note that the land observations versus HIPPO are primarily in Australia and New Zealand, whereas the ocean comparisons are in the mid-Pacific.

The NOAA aircraft network comparisons are sorted by site. Many NOAA aircraft locations are at land/ocean interfaces, allowing a more direct comparison of the land/ocean biases. On average, the AIRS land observations are 0-5 ppb higher than AIRS ocean observations at the different pressures and pressure ranges. The overall bias of AIRS versus NOAA aircraft is +7.1 ppb, whereas AIRS versus HIPPO is 4.4 ppb for the partial column matching the aircraft observations. This is consistent with AIRS land having a high bias versus ocean of 0-5 ppb.

The standard deviation of the bias for the different campaigns is a useful quantity as it is an indication of systematic error. The standard deviation of the bias varies from 4 ppb to 9 ppb for the different pressures and campaigns.

Table A.2 shows the mean bias for AIRS minus NOAA ESRL aircraft for land and ocean AIRS observations.s The different rows extend the aircraft using the AIRS prior, the CarbonTracker model (from https://www.esrl.noaa.gov/gmd/ccgg/carbontracker-ch4/ or the GEOS-Chem model (both are extended through 2018 using 2.5% secular increase). The goal of this table is to approximate the influence of the profile extension on the validation accuracy.

Table A.3 shows the standard deviation for AIRS observations minus validation data for land / ocean for different pressure ranges for both single observations and AIRS averages. The mean bias at each site is subtracted prior to calculating the standard deviation. This table shows the standard deviations for single observations and averaged quantities. The predicted error for the daily average is the observation error divided by the square root of the number of observations, and is much smaller than the actual standard deviation, indicating correlated errors. The predicted error for the monthly, 3-month, and seasonal cycle averages is the daily standard deviation divided by the square root of the number of days averaged and ~agrees with the actual standard deviation for the partial column. The location-dependent biases are subtracted from AIRS prior to calculating the standard deviation in all but the last two rows. The last two rows shows the standard deviations without

subtracting the location-dependent biases, which increases the partial column standard deviation from about 8 ppb to about 9 ppb.

Author contributions: SSK and JRW are responsible for the study design, data analysis, and manuscript writing; VHP was responsible for data analysis and manuscript editing; DF was responsible for implementing AIRS into the MUSES retrieval system; SCW and BCD were responsible for HIPPO Picarro CH_4 data; KM and CS were responsible for the ATom Picarro CH_4 data; EJD, CS, and KM were responsible for NOAA ESRL aircraft data; AL, IP, YH, and KC were responsible for implementation of the fast RT, OSS, used in this work. YY provided LMDZ model runs. DJ provided guidance on GEOS-Chem model runs.

Acknowledgements: This work is supported by NASA ROSES Aura Science Team NNN13D455T. Part of this research was carried out at the Jet Propulsion Laboratory, California Institute of Technology, under a contract with the National Aeronautics and Space Administration. The NOAA ESRL aircraft observations were obtained from http://dx.doi.org/10.25925/20190108 and supported by NOAA. The HIPPO aircraft data were obtained from http://www.eol.ucar.edu/projects/hippo/ and supported by NOAA and NSF. Thanks to Bruce Daube, Eric Kort, Jasna Pittman, Greg Santoni and others for QCLS CH_4 data collection/processing. The ATom aircraft data were obtained from https://daac.ornl.gov/ATOM/ and supported by NASA. The GEOS-Chem model output is described in Worden et al. (2013a). Thank you to helpful comments and feedback from J.D. Maasakkers.

Data Availability: AIRS methane data are available at: https://avdc.gsfc.nasa.gov/pub/data/satellite/Aura/TES/.AIRS/TROPESS/YEAR/.... Note that the field "original_species" should be used with the bias correction described in this paper.

References

Alvarado, M. J., Payne, V. H., Cady-Pereira, K. E., Hegarty, J. D., Kulawik, S. S., Wecht, K. J., Worden, J. R., Pittman, J. V. and Wofsy, S. C.: Impacts of updated spectroscopy on thermal infrared retrievals of methane evaluated with HIPPO data, Atmospheric Measurement Techniques, 8(2), 965–985, doi:10.5194/amt-8-965-2015, 2015.

Brasseur, G. P., Hauglustaine, D. A., Walters, S., Rasch, P. J., Muller, J. F., Granier, C., and Tie, X. X.: MOZART, a global chemical transport model for ozone and related chemical trac- ers 1. Model description, J. Geophys. Res.-Atmos., 103, 28265–28289, 1998.

Bowman, K. W., Rodgers, C. D., Kulawik, S. S., Worden, J., Sarkissian, E., Osterman, G., Steck, T., Lou, M., Eldering, A. and Shephard, M.: Tropospheric emission spectrometer: Retrieval method and error analysis, IEEE TRANSACTIONS ON GEOSCIENCE AND REMOTE SENSING, 44(5), 1297–1307, 2006.

Connor, B. J., B¨osch, H., Toon, G., Sen, B., Miller, C., andCrisp, D.: Orbiting Carbon Observatory: Inverse method andprospective error analysis, J. Geophys. Res., 113, A05305,doi:10.1029/2006JD008336, 2008.

Connor, T. C., Shephard, M. W., Payne, V. H., Cady-Pereira, K. E., Kulawik, S. S., Luo, M., Osterman, G., and Lampel, M.: Long-term stability of TES satellite radiance measurements, Atmos. Meas. Tech., 4, 1481–1490, https://doi.org/10.5194/amt-4-1481-2011, 2011

Cooperative Global Atmospheric Data Integration Project: Multi-laboratory compilation of atmospheric methane data for the period 1957-2017; obspack_ch4_1_GLOBALVIEWplus_v1.0_2019_01_08; NOAA, Earth System Research Laboratory, Global Monitoring Division, http://dx.doi.org/10.25925/20190108, 2019.

Crevoisier, C., Nobileau, D., Armante, R., Crépeau, L., Machida, T., Sawa, Y., Matsueda, H., Schuck, T., Thonat, T., Pernin, J., Scott, N. A. and Chedin, A.: The 2007–2011 evolution of tropical methane in the mid-troposphere as seen from space by MetOp-A/IASI, Atmospheric Chemistry and Physics, 13(8), 4279–4289, doi:10.5194/acp-13-4279-2013, 2013.

DeSouza-Machado, S., Strow, L. L., Tangborn, A., Huang, X., Chen, X., Liu, X., Wu, W. and Yang, Q.: Single-footprint retrievals for AIRS using a fast TwoSlab cloud-representation model and the SARTA all-sky infrared radiative transfer algorithm, Atmos. Meas. Tech., 11(1), 529–550, doi:10.1029/2005GL023211, 2018.

de Lange, A. and Landgraf, J.: Methane profiles from GOSAT thermal infrared spectra, Atmos. Meas. Tech., 11, 3815–3828, https://doi.org/10.5194/amt-11-3815-2018, 2018

De Wachter, E., Kumps, N., Vandaele, A. C., Langerock, B., and De Mazière, M.: Retrieval and validation of MetOp/IASI methane, Atmos. Meas. Tech., 10, 4623–4638, https://doi.org/10.5194/amt-10-4623-2017, 2017.

Folberth, G. A., Hauglustaine, D. A., Lathière, J., and Brocheton, F., Interactive chemistry in the Laboratoire de Météorologie Dynamique general circulation model: model description and impact analysis of biogenic hydrocarbons on tropospheric chemistry. Atmospheric Chemistry and Physics, 6(8), 2273–2319. https://doi.org/10.5194/acp-6-2273-2006, 2006.

Frankenberg, C., Meirink, J., Van Weele, M., Platt, U. and Wagner, T.: Assessing methane emissions from global space-borne observations, Science, 308(5724), 1010–1014, doi:10.1126/science.1106644, 2005.

Frankenberg, C., Aben, I., Bergamaschi, P., Dlugokencky, E. J., van Hees, R., Houweling, S., van der Meer, P., Snel, R. and Tol, P.: Global column-averaged methane mixing ratios from 2003 to 2009 as derived from SCIAMACHY: Trends and variability, J. Geophys. Res, 116(D4), D04302, doi:10.1029/2010JD014849, 2011.

Fu, D., Worden, J. R., Liu, X., Kulawik, S. S., Bowman, K. W. and Natraj, V.: Characterization of ozone profiles derived from Aura TES and OMI radiances, Atmospheric Chemistry and Physics, 13(6), 3445–3462, doi:10.5194/acp-13-3445-2013, 2013.

Fu, D., Bowman, K. W., Worden, H. M., Natraj, V., Worden, J. R., Yu, S., Veefkind, P., Aben, I., Landgraf, J., Strow, L., and Han, Y.: High-resolution tropospheric carbon monoxide profiles retrieved from CrIS and TROPOMI, Atmos. Meas. Tech., 9, 2567-4572579, https://doi.org/10.5194/amt-9-2567-2016, 2016.

Fu, D., Kulawik, S. S., Miyazaki, K., Bowman, K. W., Worden, J. R., Eldering, A., Livesey, N. J., Teixeira, J., Irion, F. W., Herman, R. L., Osterman, G. B., Liu, X., Levelt, P. F., Thompson, A. M. and Luo, M.: Retrievals of tropospheric ozone profiles from the synergism of AIRS and OMI: methodology and validation, Atmospheric Measurement Techniques, 11(10), 5587–5605, doi:10.5194/amt-11-5587-2018-supplement, 2018.

Fu D., Millet D.B., Wells K.C., Payne V.H., Yu S., Guenther A., and Eldering A.: Direct retrieval of isoprene from satellite-based infrared measurements, Nature Communication, 10.3811, doi:10.1038/s41467-019-11835-0. 2019.

Hu, H., Landgraf, J., Detmers, R., Borsdorff, T., Aan de Brugh, J., Aben, I., et al. (2018). Toward global mapping of methane with TROPOMI: First results and intersatellite comparison to GOSAT. Geophysical Research Letters, 45, 3682– 3689. https://doi.org/10.1002/2018GL077259

Irion, F. W., Kahn, B. H., Schreier, M. M., Fetzer, E. J., Fishbein, E., Fu, D., Kalmus, P., Wilson, R. C., Wong, S. and Yue, Q.: Single-footprint retrievals of temperature, water vapor and cloud properties from AIRS, Atmos. Meas. Tech., 11(2), 971–995, doi:10.1117/12.615244, 2018.

Kort, E. A., Patra, P. K., Ishijima, K., Daube, B. C., Jiménez, R.,Elkin, J., Hurst, D., Moore, F. L., Sweeney, C., and Wofsy,S. C.: Tropospheric distribution and variability of N2O: Evidencefor strong tropical emissions, Geophys. Res. Lett., 38, L15806,https://doi.org/10.1029/2011GL047612, 2011.

Kort, E. A., Wofsy, S. C., Daube, B. C., Diao, M., Elkins, J. W., Gao, R. S., Hintsa, E. J., Hurst, D. F., Jiménez, R., Moore, F. L., Spackman, J. R. and Zondlo, M. A.: Atmospheric observations of Arctic Ocean methane emissions up to 82° north, Nature Geoscience, 5(5), 318–321, doi:10.1038/ngeo1452, 2012.

Kort, E. A., Frankenberg, C., Costigan, K. R., Lindenmaier, R., dubey, M. K. and Wunch, D.: Four corners: The largest US methane anomaly viewed from space, Geophysical Research Letters, 10, 6898, doi:10.1002/2014GL061503, 2014.

Kulawik, S. S., Worden, H., Osterman, G., Ming Luo, Beer, R., Kinnison, D. E., Bowman, K. W., Worden, J., Eldering, A., Lampel, M., Steck, T. and Rodgers, C. D.: TES atmospheric profile retrieval characterization: an orbit of simulated observations, IEEE TRANSACTIONS ON GEOSCIENCE AND REMOTE SENSING, 44(5), 1324–1333, doi:10.1109/TGRS.2006.871207, 2006a.

Kulawik, S. S., Worden, J., Eldering, A., Bowman, K., Gunson, M., Osterman, G. B., Zhang, L., Clough, S. A., Shephard, M. W. and Beer, R.: Implementation of cloud retrievals for Tropospheric Emission Spectrometer (TES) atmospheric retrievals: part 1. Description and characterization of errors on trace gas retrievals, Journal of Geophysical Research-Atmospheres, 111, D24204, doi:10.1029/2005JD006733, 2006b.

Maasakkers, J. D., Jacob, D. J., Sulprizio, M. P., Scarpelli, T. R., Nesser, H., Sheng, J.-X., Zhang, Y., Hersher, M., Bloom, A. A., Bowman, K. W., Worden, J. R., Janssens-Maenhout, G., and Parker, R. J.: Global distribution of methane emissions, emission trends, and OH concentrations and trends inferred from an inversion of GOSAT satellite data for 2010–2015, Atmospheric Chemistry and Physics, 19(11), 7859–7881, doi:10.5194/acp-19-7859-2019, 2019.

Moncet, J-L. et al: Algorithm theoretical basis document for the Cross Track Infrared Sound er (CrIS). Volume II, Environmental Data Records (EDR), version 4.2. AER Tech. Doc. P1187-TR-I-08, 298 pp. [Available online at http://npp.gsfc.nasa.gov/sciencedocuments/2013-01/474-00056_RevABaseline.pdf.], 2005

Moncet, J-L., G. Uymin, A. E. Lipton, and H. E. Snell: Infrared radiance modeling by optimal spectral sampling. J. Atmos. Sci., 65, 3917–3934, doi: 10.1175/2008JAS2711.1, 2008

Moncet, J-L., Uymin, G., Liang, P. and Lipton, A.E: Fast and accurate radiative transfer in the thermal regime by simultaneous optimal spectral sampling over all channels. Journal of the Atmospheric Sciences, vol 72, 2622-2641, doi: 0.1175/JAS-D-14-0190.1, 2015

Pagano, T. S., Aumann, H. H., Hagan, D. E., and Overoye, K.: Prelaunch and in-flight radiometric calibration of the Atmospheric Infrared Sounder (AIRS), IEEE T. Geosci. Remote, 41, 265–273, 2003.

Parker, R., Boesch, H., Cogan, A., Fraser, A., Feng, L., Palmer, P. I., Messerschmidt, J., Deutscher, N., Griffith, D. W. T., Notholt, J., Wennberg, P. O. and Wunch, D.: Methane observations from the Greenhouse Gases Observing SATellite: Comparison to ground-based TCCON data and model calculations, Geophys. Res. Lett, 38(15), L15807, doi:10.1029/2011GL047871, 2011.

Rigby, M., Montzka, S. A., Prinn, R. G., White, J. W. C., Young, D., O'Doherty, S., Lunt, M. F., Ganesan, A. L., Manning, A. J., Simmonds, P. G., Salameh, P. K., Harth, C. M., Muehle, J., Siddans, R., Knappett, D., Kerridge, B., Waterfall, A., Hurley, J., Latter, B., Boesch, H., and Parker, R.: Global height-resolved methane retrievals from the Infrared Atmospheric Sounding Interferometer (IASI) on MetOp, Atmos. Meas. Tech., 10, 4135–4164, https://doi.org/10.5194/amt-10-4135-2017, 2017.

Pandey, S., Gautam, R., Houweling, S., van der Gon, H. D., Sadavarte, P., Borsdorff, T., Hasekamp, O., Landgraf, J., Tol, P., van Kempen, T., Hoogeveen, R., van Hees, R., Hamburg, S. P., Maasakkers, J. D., and Aben, I.: Satellite observations reveal extreme methane leakage from a natural gas well blowout, Proc Natl Acad Sci USA, 116, 26376-26381, DOI: 10.1073/pnas.1908712116, 2019.

Patra, P. K., Houweling, S., Krol, M., Bousquet, P., Belikov, D., Bergmann, D., Bian, H., Cameron-Smith, P., Chipperfield, M. P., Corbin, K., Fortems-Cheiney, A., Fraser, A., Gloor, E., Hess, P., Ito, A., Kawa, S. R., Law, R. M., Loh, Z., Maksyutov, S., Meng, L., Palmer, P. I., Prinn, R. G., Rigby, M., Saito, R., and Wilson, C.: TransCom model simulations of CH_4 and related species: linking transport, surface flux and chemical loss with CH_4 variability in the troposphere and lower stratosphere, Atmos. Chem. Phys., 11, 12813–12837, https://doi.org/10.5194/acp-11-12813-2011, 2011.

Razavi, A., Clerbaux, C., Wespes, C., Clarisse, L., Hurtmans, D., Payan, S., Camy-Peyret, C., and Coheur, P. F.: Characterization of methane retrievals from the IASI space-borne sounder, Atmos. Chem. Phys., 9, 7889–7899, https://doi.org/10.5194/acp-9-7889-2009, 2009

Rodgers, C. D.: Inverse Methods for Atmospheric Sounding: The- ory and Practice, World Sci., Tokyo, 2000.

Santoni, G. W., Daube, B. C., Kort, E. A., Jiménez, R., Park, S., Pittman, J. V., Gottlieb, E., Xiang, B., Zahniser, M. S., Nelson, D. D., McManus, J. B., Peischl, J., Ryerson, T. B., Holloway, J. S., Andrews, A. E., Sweeney, C., Hall, B., Hintsa, E. J., Moore, F. L., Elkins, J. W., Hurst, D. F., Stephens, B. B., Bent, J., and Wofsy, S. C.: Evaluation of the airborne quantum cascade laser

spectrometer (QCLS) measurements of the carbon and greenhouse gas suite – CO_2, CH_4, N_2O, and CO – during the CalNex and HIPPO campaigns, Atmos. Meas. Tech., 7, 1509–1526, https://doi.org/10.5194/amt-7-1509-2014, 2014.

Schepers, D., Guerlet, S., Butz, A., Landgraf, J., Frankenberg, C., Hasekamp, O., Blavier, J.-F., Deutscher, N. M., Griffith, D. W. T., Hase, F., Kyro, E., Morino, I., Sherlock, V., Sussmann, R., and Aben, I.: Methane retrievals from Greenhouse Gases Observing Satellite (GOSAT) shortwave infrared measurements: performance comparison of proxy and physics retrieval algorithms, J. Geophys. Res., 117, D10307, doi:10.1029/2012JD017549, 2012.

Shephard, M.W., Worden, H.M., Cady-Pereira, K.E., Lampel, M., Luo, M., Bowman, K.W., Sarkissian, E., Beer, R., Rider, D.M., Tobin, D.C., Revercomb, H.E., Fisher, B.M., Tremblay, D., Clough, S.A., Osterman, G.B., and Gunson, M., Tropospheric Emission Spectrometer nadir spectral radiance comparisons, J. Geophys. Res., 113, D15S05, doi:10.1029/2007JD008856, 2008.

Siddans, R., Knappett, D., Kerridge, B., Waterfall, A., Hurley, J., Latter, B., Boesch, H., and Parker, R.: Global height-resolved methane retrievals from the Infrared Atmospheric Sounding Interferometer (IASI) on MetOp, Atmos. Meas. Tech., 10, 4135–4164, https://doi.org/10.5194/amt-10-4135-2017, 2017.

Smith, N. and Barnet, C. D. (2019), Uncertainty characterization and propagation in the Community Long-Term Infrared Microwave Combined Atmospheric Product System (CLIMCAPS), Remote Sens., 11, doi:10.3390/rs11101227

Turner, A. J., Frankenberg, C. and Kort, E. A.: Interpreting contemporary trends in atmospheric methane, Proceedings of the National Academy of Sciences of the United States of America, 8(8), 201814297–9, doi:10.1073/pnas.1814297116, 2019.

Turner, A. J., Fung, I., Naik, V., Horowitz, L. W. and Cohen, R. C.: Modulation of hydroxyl variability by ENSO in the absence of external forcing, Proceedings of the National Academy of Sciences of the United States of America, 115(36), 8931–8936, doi:10.1073/pnas.1807532115, 2018a.

Turner, A. J., Jacob, D. J., Benmergui, J., Brandman, J., White, L. and Randles, C. A.: Assessing the capability of different satellite observing configurations to resolve the distribution of methane emissions at kilometer scales, Atmospheric Chemistry and Physics, 18(11), 8265–8278, doi:10.5194/acp-18-8265-2018, 2018b.

Turner, A.J., D.J. Jacob, K.J. Wecht, J.D. Maasakkers, E. Lundgren, A.E. Andrews, S.C. Biraud, H. Boesch, K.W. Bowman, N.M. Deutscher, M.K. Dubey, D.W.T. Griffith, F. Hase, A. Kuze, J. Notholt, H. Ohyama, R. Parker, V.H. Payne, R. Sussmann, C. Sweeney, V.A. Velazco, T. Warneke, P.O. Wennberg, and D. Wunch Estimating global and North American methane emissions with high spatial resolution using GOSAT satellite data, Atmos. Chem. Phys., 15, 7049-7069, 2015.

Varon, D. J., McKeever, J., Jervis, D., Maasakkers, J. D., Pandey, S., Houweling, S., et al. (2019). Satellite discovery of anomalously large methane point sources from oil/gas production. Geophysical Research Letters, 46, 13507– 13516. https://doi.org/10.1029/2019GL083798

Wecht, K. J., Jacob, D. J., Wofsy, S. C., Kort, E. A., Worden, J. R., Kulawik, S. S., Henze, D. K., Kopacz, M. and Payne, V. H.: Validation of TES methane with HIPPO aircraft observations: implications for inverse modeling of methane sources, Atmospheric Chemistry and Physics, 12(4), 1823–1832, doi:10.5194/acp-12-1823-2012, 2012.

Wecht, K. J., Jacob, D. J. and Sulprizio, M. P.: Spatially resolving methane emissions in California: constraints from the CalNex aircraft campaign and from present (GOSAT, TES) and future (TROPOMI) missions, Atmospheric Chemistry and Physics, doi:10.5194/acp-14-8173-2014, 2014.

Wofsy, S. C., B. C. Daube, R. Jimenez, E. Kort, J. V. Pittman, S. Park, R. Commane, B. Xiang G. Santoni, D. Jacob, J. Fisher, C. Pickett-Heaps, H. Wang, K. Wecht, Q.-Q. Wang, B. B. Stephens, S. Shertz, A.S. Watt, P. Romashkin, T. Campos, J. Haggerty, W. A. Cooper, D. Rogers, S. Beaton, R. Hendershot, J. W. Elkins, D. W. Fahey, R. S. Gao, F. Moore, S. A. Montzka, J. P. Schwarz, A. E. Perring, D. Hurst, B. R. Miller, C. Sweeney, S. Oltmans, D. Nance, E. Hintsa, G. Dutton, L. A. Watts, J. R. Spackman, K. H. Rosenlof, E. A. Ray, B. Hall, M. A. Zondlo, M. Diao, R. Keeling, J. Bent, E. L. Atlas, R. Lueb, M. J. Mahoney. HIPPO Merged 10-second Meteorology, Atmospheric Chemistry Aerosol Data (R_20121129), Carbon Dioxide Information Analysis Center, Oak Ridge National Laboratory, Oak Ridge, Tennessee U.S.A., 2012.

Wofsy, S.C., and ATom Science Team. ATom: Aircraft Flight Track and Navigational Data. ORNL DAAC, Oak Ridge, Tennessee, USA, 2018. https://doi.org/10.3334/ORNLDAAC/1613

Worden, J., Kulawik, S., Shepard, M., Clough, S., Worden, H., Bowman, K. and Goldman, A.: Predicted errors of tropospheric emission spectrometer nadir retrievals from spectral window selection, Journal of Geophysical Research-Atmospheres, 109(D9), D09308, doi:10.1029/2004JD004522, 2004.

Worden, J., Noone, D., Galewsky, J., Bailey, A., Bowman, K., Brown, D., Hurley, J., Kulawik, S., Lee, J. and Strong, M.: Estimate of bias in Aura TES HDO/H2O profiles from comparison of TES and in situ HDO/H2O measurements at the Mauna Loa observatory, Atmospheric Chemistry and Physics, 11(9), 4491–4503, doi:10.5194/acp-11-4491-2011, 2011.

Worden, J., Kulawik, S., Frankenberg, C., Payne, V., Bowman, K., Cady-Peirara, K., Wecht, K., Lee, J.-E., and Noone, D.: Profiles of CH_4, HDO, H_2O, and N_2O with improved lower tropospheric vertical resolution from Aura TES radiances, Atmos. Meas. Tech., 5, 397-411, https://doi.org/10.5194/amt-5-397-2012, 2012.

Worden, J., K. Wecht, C. Frankenberg, M. Alvarado, K. Bowman, E. Kort, S. Kulawik, M. Lee, V. Payne, and H. Worden, CH_4 and CO distributions over tropical fires during October 2006 observed by the Aura TES satellite instrument and modeled by GEOS-Chem, Atmospheric Chemistry and Physics, 13(7), 3679–3692, doi:10.5194/acp-13-3679-2013, 2013a.

Worden, J., Jiang, Z., Jones, D. B. A., Alvarado, M., Bowman, K., Frankenberg, C., Kort, E. A., Kulawik, S. S., Lee, M., Liu, J., Payne, V., Wecht, K. and Worden, H.: El Nino, the 2006 Indonesian Peat Fires, and the distribution of atmospheric methane, Geophys. Res. Lett, 40, 1, doi:10.1002/grl.50937, 2013b.

Worden, J. R., Turner, A. J., Bloom, A., Kulawik, S. S., Liu, J., Lee, M., Weidner, R., Bowman, K., Frankenberg, C., Parker, R., and Payne, V. H.: Quantifying lower tropospheric methane concentrations using GOSAT near-IR and TES thermal IR measurements, Atmos. Meas. Tech., 8, 3433-3445, https://doi.org/10.5194/amt-8-3433-2015, 2015.

Worden, J. R., Bloom, A. A., Pandey, S., Jiang, Z., Worden, H. M., Walker, T. W., Houweling, S. and Röckmann, T.: Reduced biomass burning emissions reconcile conflicting estimates of the post-2006 atmospheric methane budget, Nat Commun, 1–11, doi:10.1038/s41467-017-02246-0, 2017a.

Worden, J. R., Doran, G., Kulawik, S., Eldering, A., Crisp, D., Frankenberg, C., O amp apos Dell, C. and Bowman, K.: Evaluation and attribution of OCO-2 XCO2 uncertainties, Atmospheric Measurement Techniques, 10(7), 2759–2771, doi:10.5194/amt-10-2759-2017, 2017b.

Worden, J. R., Kulawik, S. S., Fu, D., Payne, V. H., Lipton, A. E., Polonsky, I., He, Y., Cady-Pereira, K., Moncet, J.-L., Herman, R. L., Irion, F. W. and Bowman, K. W.: Characterization and evaluation of AIRS-based estimates of the deuterium content of water vapor, Atmospheric Measurement Techniques, 12(4), 2331–2339, doi:10.5194/amt-12-2331-2019, 2019.

Wunch, D., Toon, G. C., Wennberg, P. O., Wofsy, S. C., Stephens, B. B., Fischer, M. L., Uchino, O., Abshire, J. B., Bernath, P., Biraud, S. C., Blavier, J.-F. L., Boone, C., Bowman, K. P., Browell, E. V., Campos, T., Connor, B. J., Daube, B. C., Deutscher, N. M., Diao, M., Elkins, J. W., Gerbig, C., Gottlieb, E., Griffith, D. W. T., Hurst, D. F., Jiménez, R., Keppel-Aleks, G., Kort, E. A., Macatangay, R., Machida, T., Matsueda, H., Moore, F., Morino, I., Park, S., Robinson, J., Roehl, C. M., Sawa, Y., Sherlock, V., Sweeney, C., Tanaka, T., and Zondlo, M. A.: Calibration of the Total Carbon Column Observing Network using aircraft profile data, Atmos. Meas. Tech., 3, 1351–1362, https://doi.org/10.5194/amt-3-1351-2010, 2010.

Xiong, X., Barnet, C., Maddy, E., Wofsy, S. C., Chen, L. A., Karion, A. and Sweeney, C.: Detection of methane depletion associated with stratospheric intrusion by atmospheric infrared sounder (AIRS), Geophysical Research Letters, 40(10), 2455–2459, doi:10.1002/grl.50476, 2013.

Xiong, X., Houweling, S., Wei, J., Maddy, E., Sun, F. and Barnet, C.: Methane plume over south Asia during the monsoon season: satellite observation and model simulation, Atmospheric Chemistry and Physics, 9(3), 783–794, 2009.

Xiong X, Han Y, Liu Q and Weng F, Comparison of atmospheric methane retrievals from AIRS and IASI IEEE J. Sel. Top. Appl. Earth Obs. Remote Sens. 9 3297–303, 2016.

Xiong, X., Weng, F., Liu, Q., and Olsen, E.: Space-borne observation of methane from atmospheric infrared sounder version 6: validation and implications for data analysis, Atmos. Meas. Tech. Discuss., 8, 8563–8597, https://doi.org/10.5194/amtd-8-8563-2015, 2015.

Zhang, Y., Jacob, D. J., Maasakkers, J. D., Sulprizio, M. P., Sheng, J.-X., Gautam, R. and Worden, J.: Monitoring global tropospheric OH concentrations using satellite observations of atmospheric methane, Atmospheric Chemistry and Physics, 18(21), 15959–15973, doi:10.1029/2007JG000500, 2018.

Table 1. Bias versus pressure with and without bias correction. The bias correction was developed on HIPPO-4 and tested on HIPPO-4; HIPPO-1,2,3,5; and NOAA aircraft network.

Pressure (hPa)	AIRS minus aircraft_AK (HIPPO-4) (ppb)	After bias correction (HIPPO-4) (ppb)	After bias correction (all HIPPO except HIPPO-4) (ppb)	After bias correction (all NOAA) (ppb)
1000	24	-1	-3	1
824	36	0	-4	1
681	48	1	-5	2
562	58	1	-4	2
464	60	-5	-3	3
383	67	-5	-2	2
316	81	1	4	-
261	86	1	4	-
215	89	1	3	-
161	-	-	4	-

675 Table A.1 Bias by campaign, station, land/ocean, and pressure.

Station/campaign	Location	Time period	Bias 700 hPa (ppb)	Bias 500 hPa (ppb)	Bias 300 hPa (ppb)	Bias column matching aircraft (ppb)	Bias column above 750 hPa (ppb)
HIPPO 1S	Pacific	Jan, 2009	-6.2	2.4	11.0	4.2	6.3
HIPPO 1N	Pacific	Jan, 2009	-3.2	3.7	12.5	-0.1	4.8
HIPPO 2S	Pacific	Nov, 2009	-9.0	-0.4	9.8	-4.4	5.0
HIPPO 2N	Pacific	Nov, 2009	-4.3	-3.3	-3.1	-4.0	-4.0
HIPPO 3N	Pacific	Apr, 2010	-8.5	1.1	16.5	-2.6	2.6
HIPPO 4S	Pacific	Jun, 2011	-0.7	-2.0	9.5	1.8	10.2
HIPPO 4N	Pacific	Jul, 2011	8.7	11.8	0.7	8.7	7.3
HIPPO 5S	Pacific	Aug, 2011	1.2	7.6	13.3	4.5	9.3
HIPPO 5N	Pacific	Sep, 2011	-5.2	0.5	1.2	-2.0	2.2
HIPPO all land	**-**	**-**	**10.9**	**18.2**	**17.8**	**16.1**	**14.8**
HIPPO all ocean	**-**	**-**	**-5.2**	**-0.9**	**4.3**	**-1.7**	**3.1**
HIPPO all (mean)	**-**	**-**	**-2.9**	**2.1**	**7.9**	**0.7**	**4.9**
HIPPO all (stdev)	**-**	**-**	**5.9**	**5.2**	**6.7**	**4.4**	**4.3**
ACG	68N, 152W	-	21.4	-	-	18.6	26.7
ESP	49N, 126W	-	9.7	-	-	8.2	13.8
NHA	43N, 71W	-	15.7	23.8	-	15.7	19.3
THD	41N, 124W	-	13.6	21.7	-	14.0	21.2
CMA	39N, 74W	-	-0.2	5.7	-	0.9	3.6
TGC	28N, 97W	-	1.0	7.9	-	2.3	6.5
RTA	21S, 160W	-	3.7	11.5	-	3.9	12.8
ESRL all land	**-**	**-**	**9.2**	**16.8**	**-**	**9.4**	**14.3**
ESRL all ocean	**-**	**-**	**9.0**	**12.8**	**-**	**8.7**	**15.4**

ESRL all (mean)	**-**	**-**	**9.3**	**14.1**	**-**	**9.1**	**14.8**
ESRL all (stdev)	**-**	**-**	**8.1**	**8.2**	**-**	**7.1**	**8.2**
ATom 1S	Pacific	Aug, 2016	-0.2	4.5	7.7	2.0	3.5
ATom 1N	Atlantic	Aug, 2016	0.2	3.2	13.2	2.8	6.9
ATom 2S	Pacific	Feb, 2017	-6.8	0.7	8.4	-2.5	5.2
ATom 2N	Atlantic	Feb, 2017	5.7	12.3	25.3	8.3	12.5
ATom 3S	Pacific	Oct, 2017	-2.5	3.0	9.1	0.9	5.9
ATom 3N	Atlantic/Pacific	Oct, 2017	6.5	13.0	21.9	9.3	13.8
ATom 4S	Pacific	April/May, 2018	-0.1	3.9	9.4	2.3	6.0
ATom 4N	Atlantic	May, 2018	-1.4	5.9	23.4	3.4	13.2
ATom all land	**-**	**-**	**16.7**	**23.6**	**26.2**	**17.0**	**18.2**
ATom all ocean	**-**	**-**	**-3.2**	**2.4**	**13.4**	**0.6**	**6.5**
ATom all (mean)	**-**	**-**	**0.1**	**5.8**	**14.7**	**3.2**	**8.3**
ATom all (stdev)	**-**	**-**	**4.3**	**4.5**	**7.5**	**3.8**	**4.1**

Table A.2 Change in the mean bias of the partial column matching the aircraft observation using different aircraft profile extensions from the top aircraft measurement to the top of the atmosphere.

Quantity	Profile extension	Bias 700 hPa (ppb)	Bias 500 hPa (ppb)	Bias 300 hPa (ppb)	Bias column matching aircraft (ppb)	Bias column above 750 hPa (ppb)
Land ESRL	CT	6.0	10.3	-	6.1	3.8
Ocean ESRL	CT	4.5	5.7	-	4.3	4.0
Land ESRL	prior	9.2	16.8	-	9.4	14.3
Ocean ESRL	prior	9.0	12.8	-	8.7	15.4
Land ESRL	GEOS-Chem	6.4	11.7	-	6.7	6.4
Ocean ESRL	GEOS-Chem	4,4	7.7	-	4.5	6.4

Table A.3 Standard deviation of AIRS minus validation for land / ocean observations and different pressures / pressure ranges. Rows 1-2 show the standard deviation for single observation, rows 3-4 show the predicted observation error, rows 5-8 show the standard deviation for daily averages, rows 9-10 show the predicted error for daily averages (assuming random error), rows 11-12 show the standard deviation for 3-month averages, rows 13-14 show the standard deviation for seasonal cycle averages (average the same month of all years), rows 15-16 show the predicted error for the seasonal cycle averages, and rows 17-18 show the standard deviation without bias subtraction. The site-dependent biases from Table A.1 are subtracted prior to calculating the standard deviation.

Quantity	Stdev 700 hPa (ppb)	Stdev 500 hPa (ppb)	Stdev 300 hPa (ppb)	**Stdev column matching aircraft (ppb)**	Stdev column above 750 hPa (ppb)
Land single	26	29	26	**23**	25
Ocean single	25	27	26	**22**	24
Land observation error	26	26	19	**23**	19
Ocean observation error	28	28	20	**24**	19
Land daily (≥3 obs/day)	17	21	16	**15**	20
Ocean daily (≥3 obs/day)	18	21	21	**16**	20
Land daily (≥9 obs/day)	16	20	16	**14**	20
Ocean daily (≥9 obs/day)	17	19	21	**15**	18
Land daily (≥9 obs/day) pred.	9.7	9.9	5.7	**8.5**	7.0
Ocean daily (≥9 obs/day) pred.	8.4	7.9	4.6	**7.0**	5.7
Land 3-month (≥3 obs/day, ≥3 days)	9.5	13.3	-	**8.8**	12.9
Ocean 3-month (≥3 obs/day, ≥3 days)	9.0	11.8	-	**8.3**	11.8
Land monthly (average all years)	8.3	11.8	-	**7.7**	10.7
Ocean monthly (average all years)	8.3	10.4	-	**7.5**	10.1
Land monthly (average all years) pred.	7.7	9.9	-	**6.9**	9.3

Ocean monthly (average all years) pred.	8.0	9.8	-	**7.2**	9.5
Land monthly (average all years) without bias subtraction	9.9	13.7	-	**9.1**	12.2
Ocean monthly (average all years) without bias subtraction	10.4	12.3	-	**9.4**	11.6

690

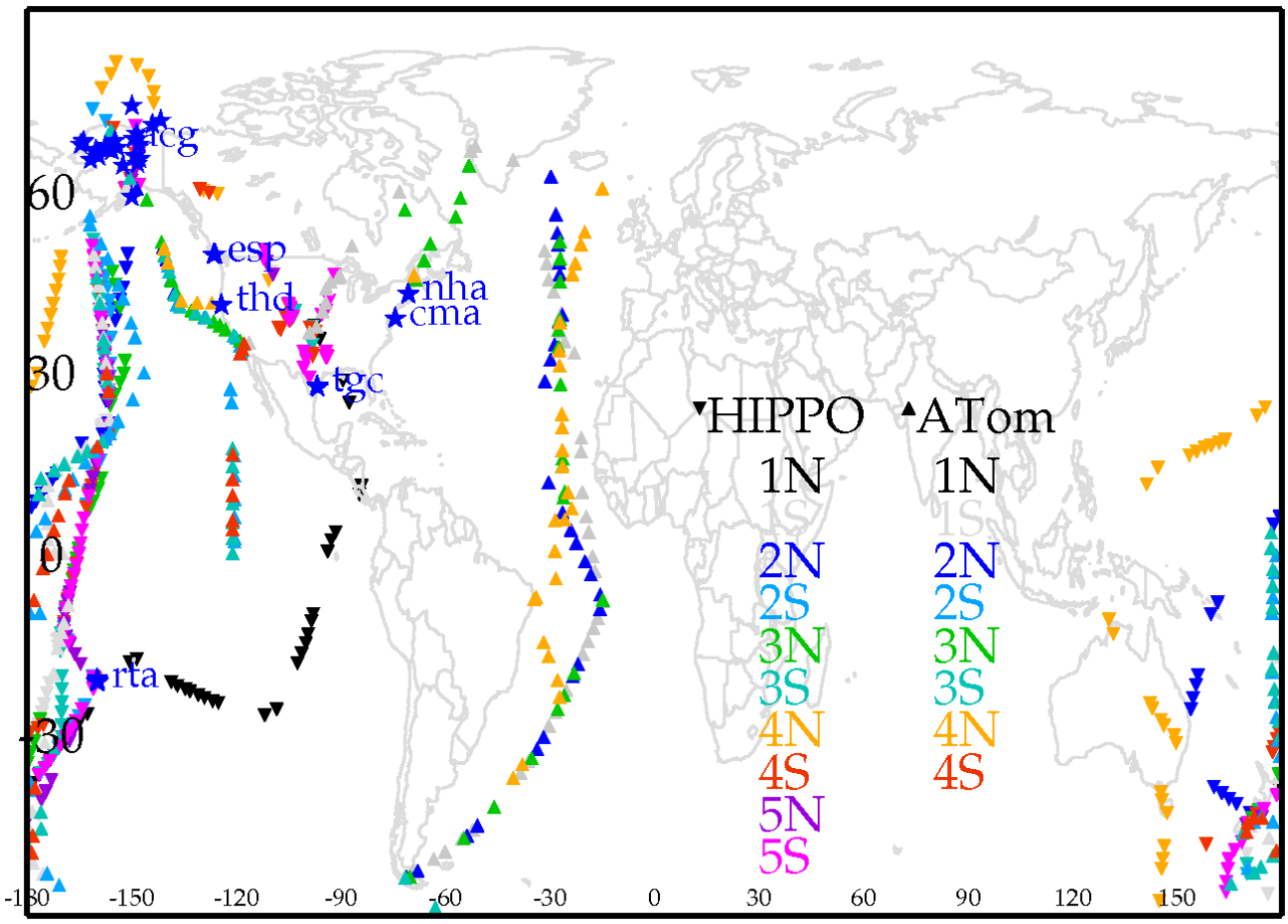

Figure 1: Location of aircraft profile measurements used for validation. The upside-down triangles show HIPPO, triangles show ATom, and blue stars show NOAA ESRL aircraft validation locations.

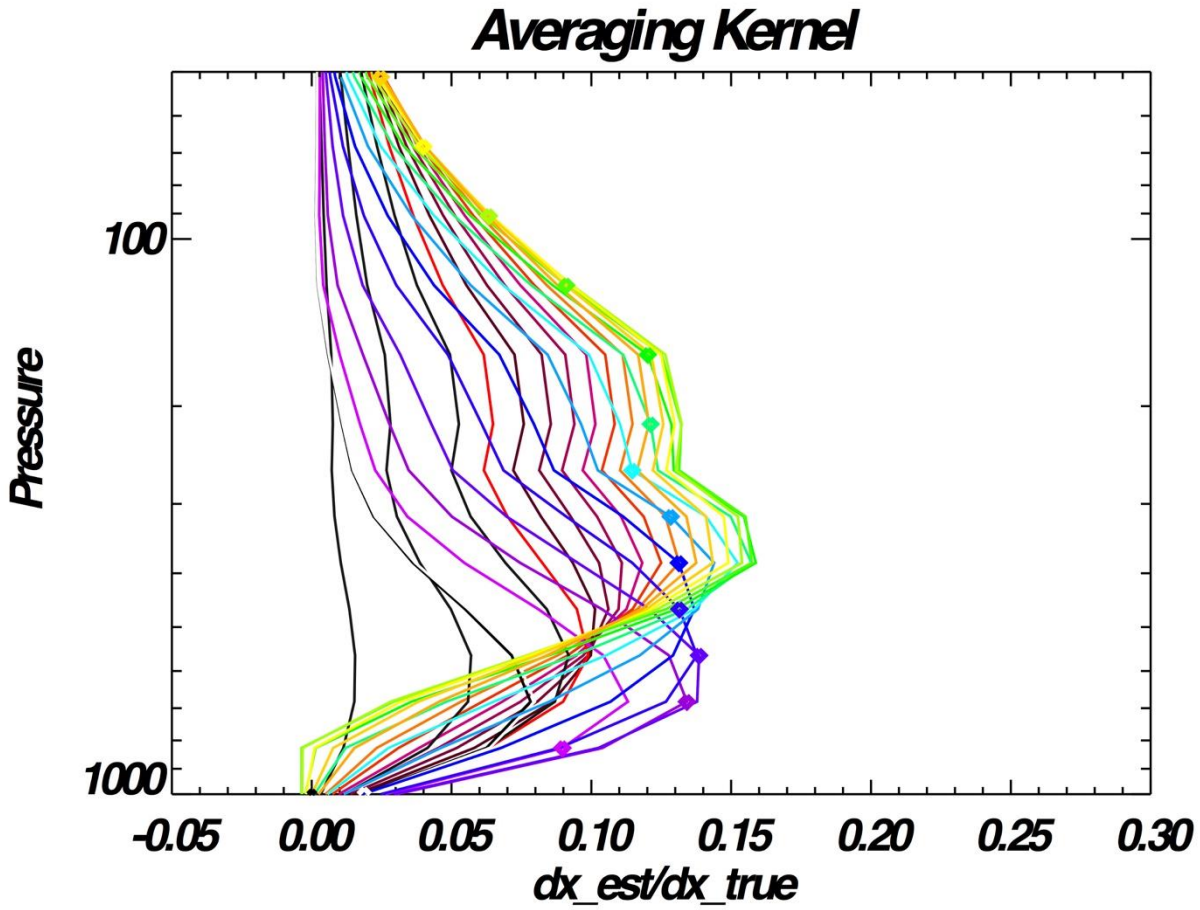

Figure 2: The rows of an averaging kernel for CH_4 for a tropical scene. The colors help for visualization of the pressure levels for each row of the averaging kernel. The diamonds indicate the pressure level corresponding to the row of the averaging kernel.

700

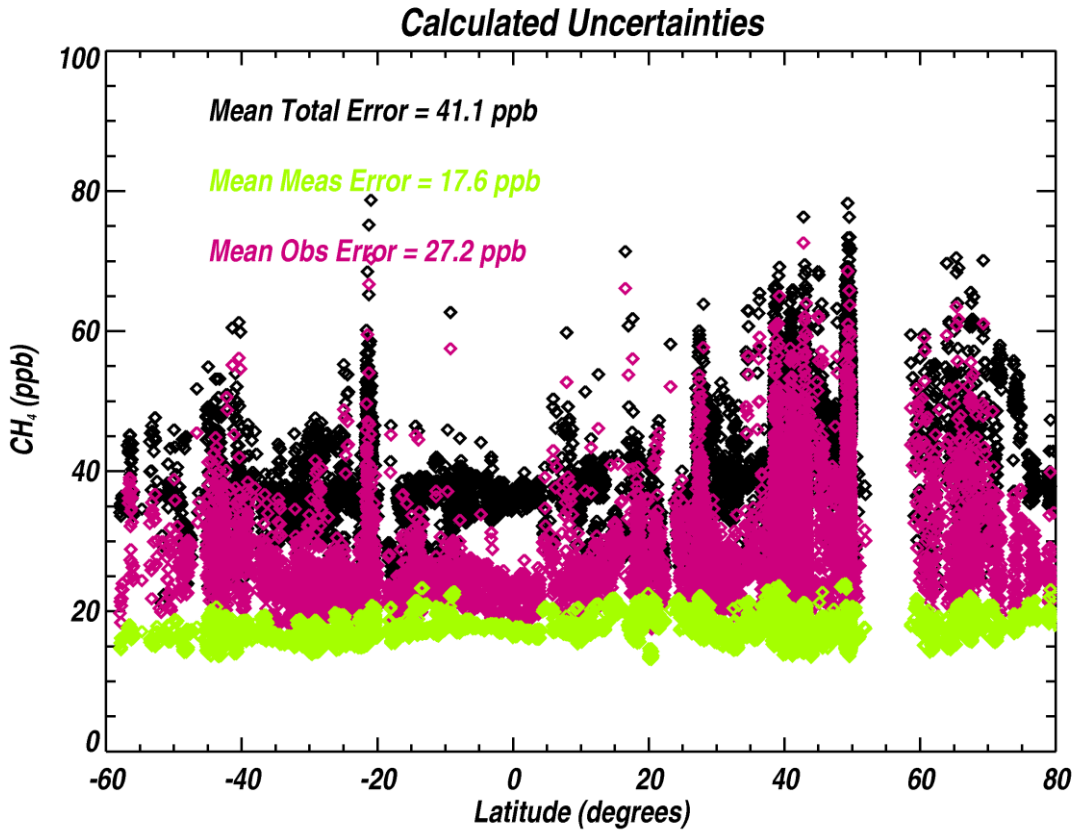

Figure 3: Calculated errors for AIRS measurements shown in this paper.

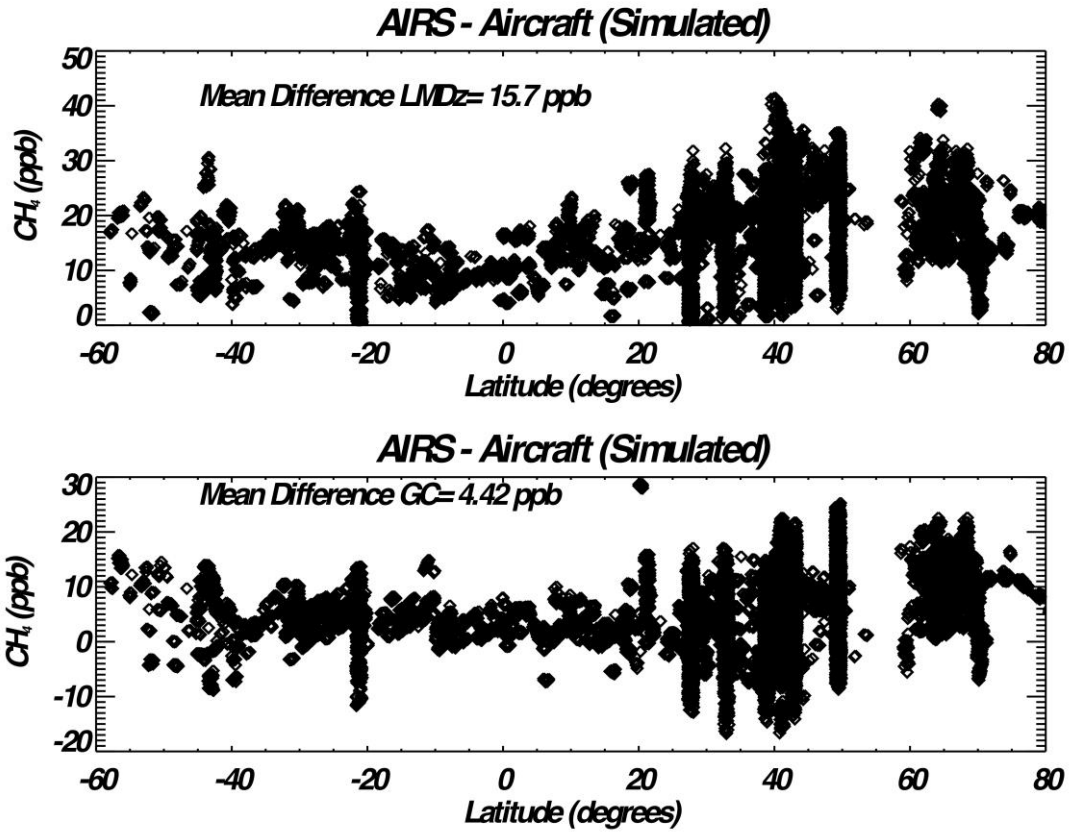

705

Figure 4: Simulated comparison between AIRS and Aircraft in which the LMDz model (top) and GEOS-Chem model (bottom) are used for the simulation.

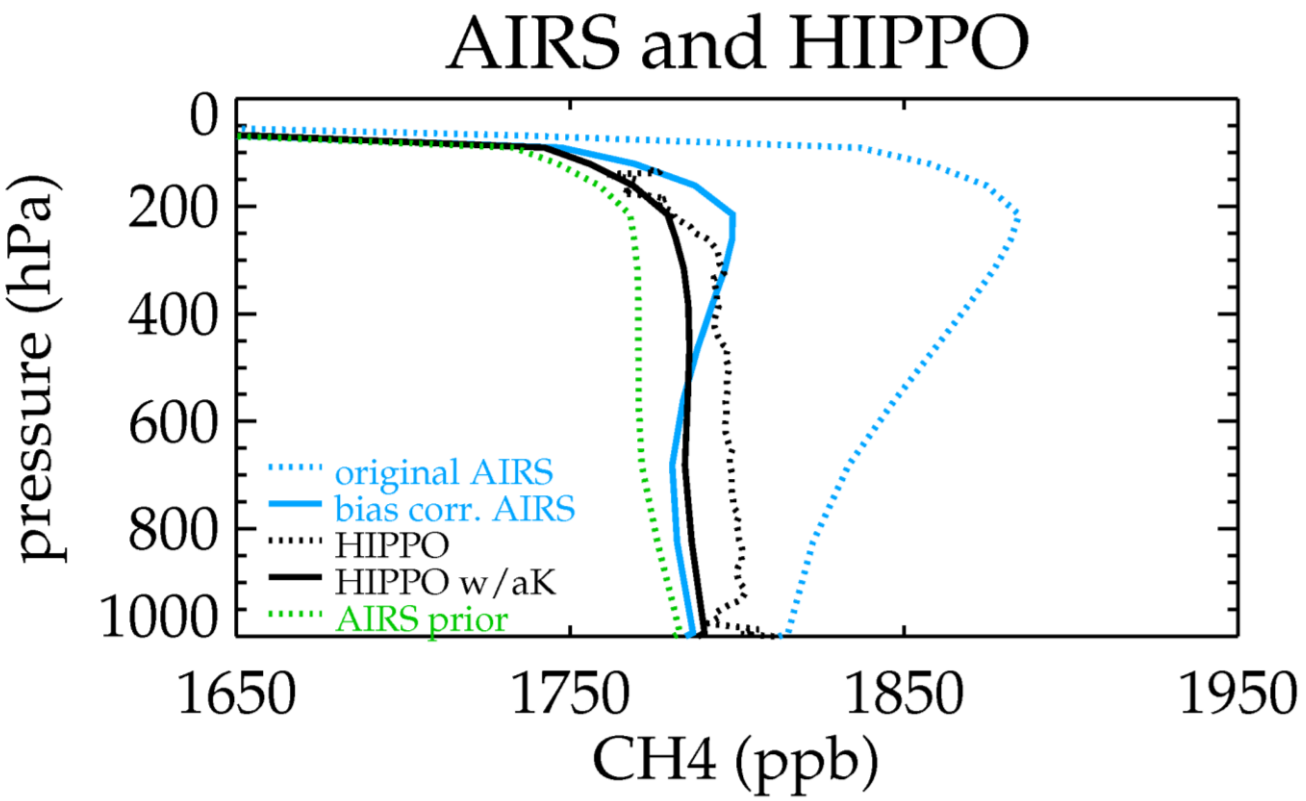

Figure 5: Example of the effect of bias correction on the AIRS profile from averaged HIPPO-1,2,3,5. The blue lines shows the AIRS methane profile before (dotted) and after (solid) bias correction. The black line shows the HIPPO measurements before (dotted) and after averaging kernel is applied (solid).

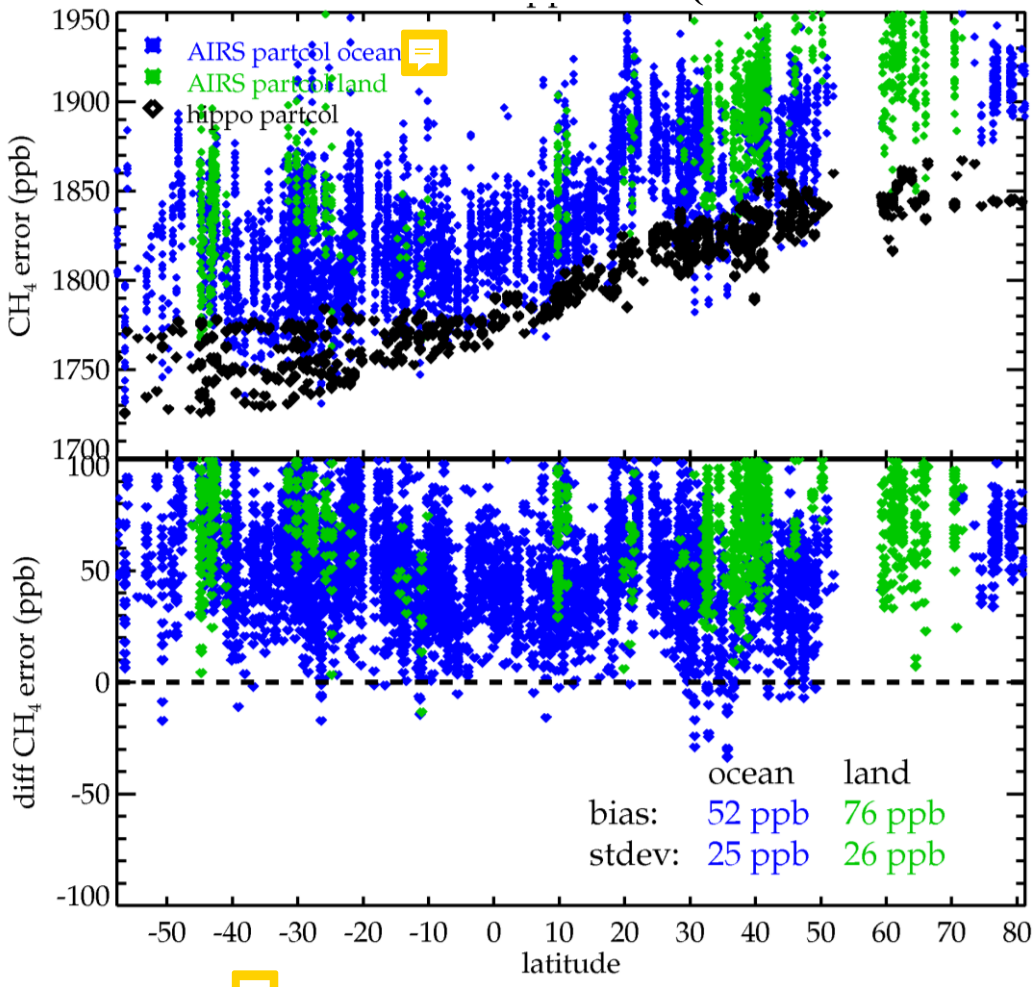

715 **Figure 6: Comparison of AIRS methane to aircraft for all HIPPO comparisons over the partial column range measured by the aircraft. Blue shows AIRS ocean observations and green shows AIRS land observations.**

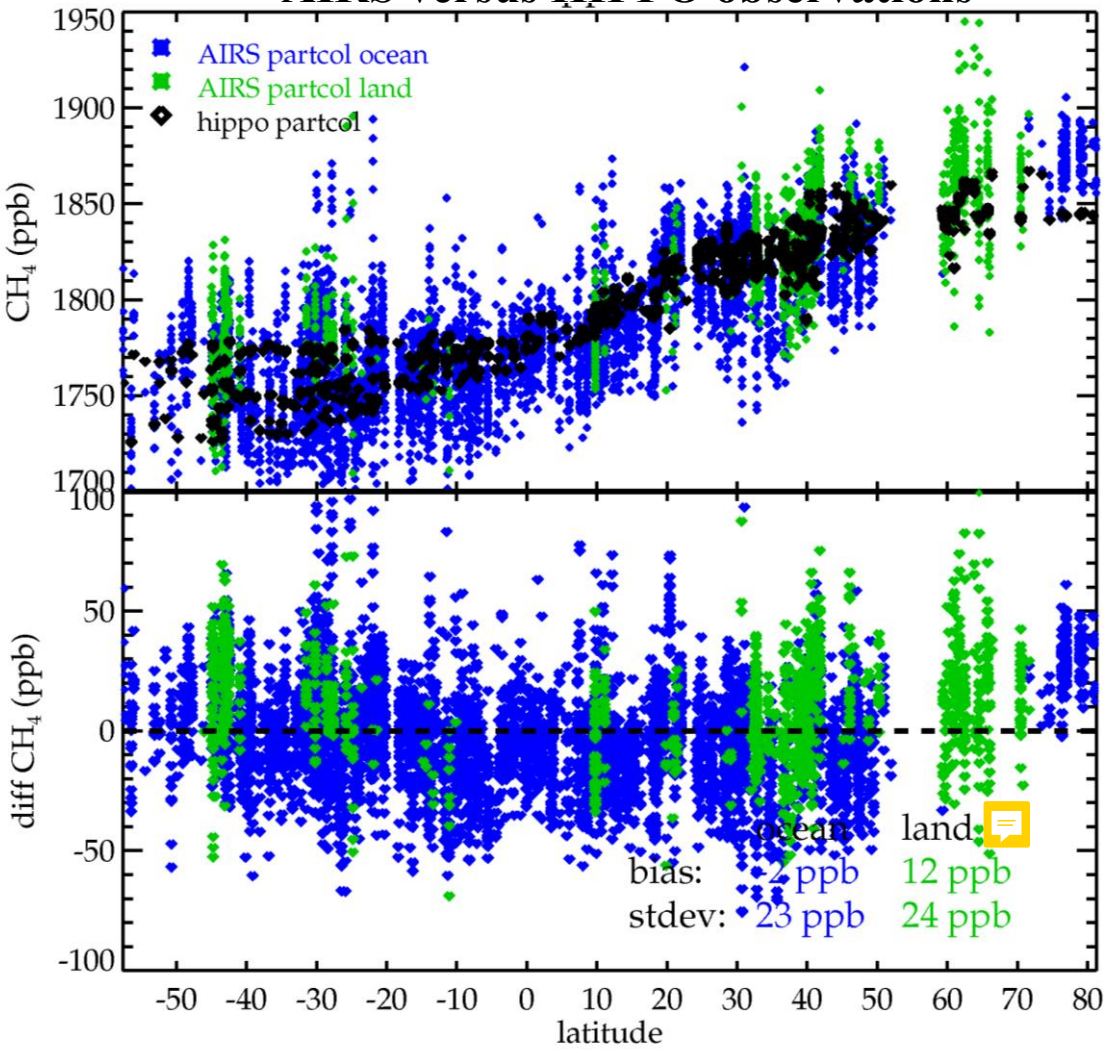

Figure 7: Same as Figure 6 but after bias correction

720

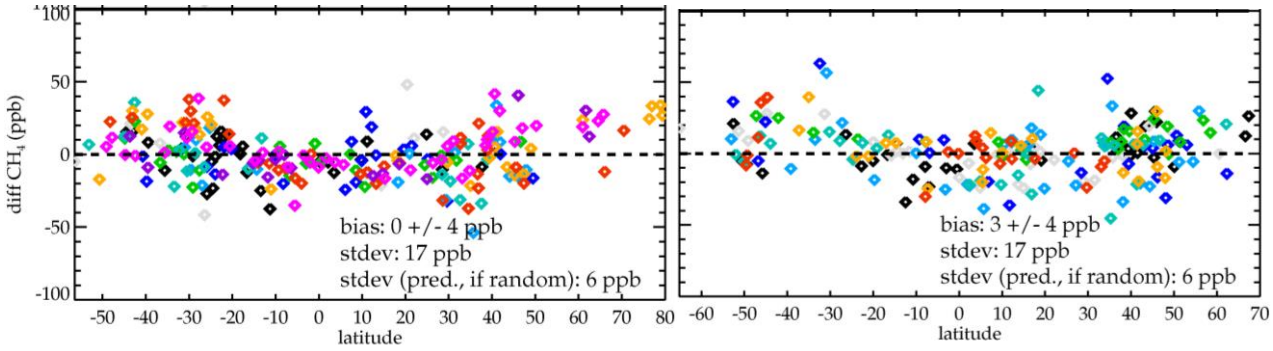

Figure 8: Comparison of daily averaged AIRS to HIPPO measurements (left) and ATom measurements (right) for the partial column observed by the aircraft. The different colors correspond to the campaigns shown in Fig. 1

725

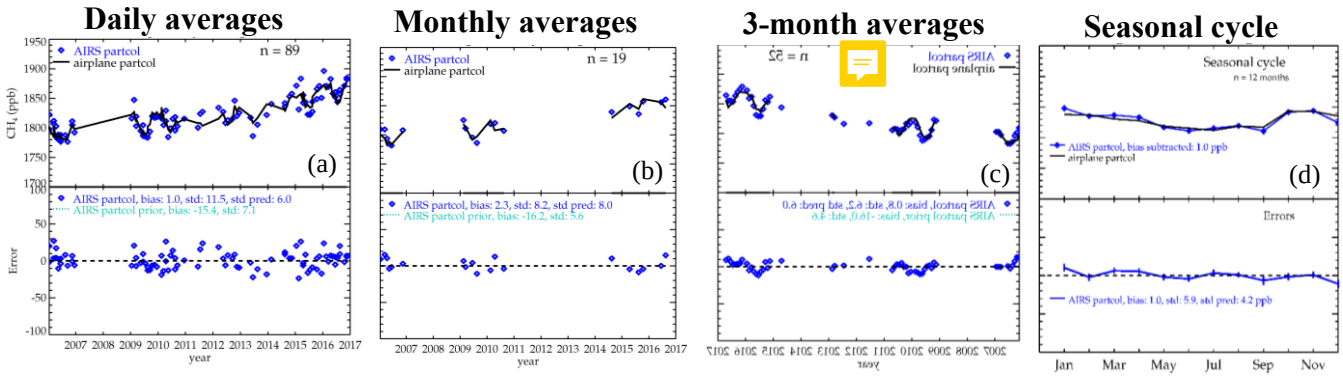

Figure 9: Comparison at TGC (27.7N, 96.9E). (Top) Comparison of AIRS and co-located NOAA aircraft flights in SE Texas for the partial column measured by the aircraft. Data are averaged over 1 day (a), 1 month (b), 90-days (c), and averaged over month from all years (d). (Bottom) Difference from the aircraft. The predicted error for daily observations is the observation error (27 ppb) divided by the square root of the number of observations. The predicted monthly or seasonal error is the mean daily error (11.5 ppb) divided by the square root of the number of days averaged.